A20 regulates lymphocyte adhesion in murine neuroinflammation by restricting endothelial ICOSL expression in the CNS
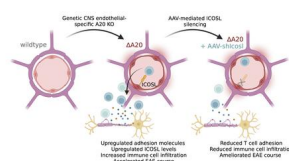
Lisa Johann, … , Markus Schwaninger, Ari Waisman

Research In-Press Preview   Autoimmunity   Neuroscience

Graphical abstract

Find the latest version:

https://jci.me/168314/pdf

1   A20 regulates lymphocyte adhesion in murine neuroinflammation by restricting endothelial

2   ICOSL expression in the CNS

3

4   Lisa Johann[1], Sasha Soldati[2], Kristin Müller[3], Josephine Lampe[3,4], Federico Marini[5,6], Matthias

5   Klein[7], Eva Schramm[1], Nathalie Ries[1], Carsten Schelmbauer[1], Ilaria Palagi[1], Khalad Karram[1],

6   Julian C. Assmann[3], Mahtab A. Khan[3], Jan Wenzel[3,4], Mirko H. H. Schmidt[8], Jakob Körbelin[9],

7   Dirk Schlüter[10], Geert van Loo[11,12], Tobias Bopp[6,7], Britta Engelhardt[2], Markus Schwaninger[3,4]

8   and Ari Waisman[1,6]

9

10   [1] Institute for Molecular Medicine, University Medical Center of the Johannes Gutenberg

11   University Mainz, Mainz, Germany

12   [2] Theodor Kocher Institute, University of Bern, Bern, Switzerland

13   [3] Institute for Experimental and Clinical Pharmacology and Toxicology, Center of Brain,

14   Behavior and Metabolism (CBBM), University of Lübeck, Lübeck, Germany

15   [4] DZHK (German Research Centre for Cardiovascular Research), Hamburg-Lübeck-Kiel,

16   Germany

17   [5] Institute of Medical Biostatistics, Epidemiology and Informatics (IMBEI), University Medical

18   Center of the Johannes Gutenberg University Mainz, Mainz, Germany

19   [6] Research Center for Immunotherapy (FZI), University Medical Center of the Johannes

20   Gutenberg University Mainz, Mainz, Germany

21   [7] Institute for Immunology, University Medical Center of the Johannes Gutenberg University

22   Mainz, Mainz, Germany

23   [8] Institute of Anatomy, Medical Faculty Carl Gustav Carus, Technische Universität Dresden

24   School of Medicine, Dresden, Germany

25   [9] University Medical Center Hamburg-Eppendorf, Department of Oncology, Hematology and

26   Bone Marrow Transplantation, Hamburg, Germany

27   [10] Hannover Medical School, Institute of Medical Microbiology and Hospital Epidemiology,

28   Hannover, Germany

29   [11] Department of Biomedical Molecular Biology, Ghent University, Ghent, Belgium

30   [12] VIB-UGent Center for Inflammation Research, Ghent, Belgium

31

32
33   Corresponding author:

34   Ari Waisman

35   Institute for Molecular Medicine, University Medical Center of the Johannes Gutenberg

36   University Mainz, Langenbeckstraße 1, 55131 Mainz, Germany

37   (+49) 6131-17-9129

38   waisman@uni-mainz.de

39

43

44 ABSTRACT

45 A20 is a ubiquitin-modifying protein that negatively regulates NF-κB signaling. Mutations in

46 A20/*TNFAIP3* are associated with a variety of autoimmune diseases, including multiple

47 sclerosis (MS). We found that deletion of A20 in central nervous system (CNS) endothelial cells

48 (ECs) enhances experimental autoimmune encephalomyelitis (EAE), a mouse model of MS.

49 A20$^{\Delta CNS-EC}$ mice showed increased numbers of CNS-infiltrating immune cells during

50 neuroinflammation and in the steady state. While the integrity of the blood-brain barrier

51 (BBB) was not impaired, we observed a strong activation of CNS-ECs in these mice, with

52 dramatically increased levels of the adhesion molecules ICAM-1 and VCAM-1. We discovered

53 ICOSL as adhesion molecule expressed by A20-deficient CNS-ECs. Silencing of ICOSL in CNS

54 microvascular ECs partly reversed the phenotype of A20$^{\Delta CNS-EC}$ mice without reaching

55 statistical significance and delayed the onset of EAE symptoms in wildtype mice. In addition,

56 blocking of ICOSL on primary mouse brain microvascular endothelial cells (pMBMECs)

57 impaired the adhesion of T cells in vitro. Taken together, we here propose that CNS EC-ICOSL

58 contributes to the firm adhesion of T cells to the BBB, promoting their entry into the CNS and

59 eventually driving neuroinflammation.

60

64 INTRODUCTION

65 Multiple sclerosis (MS) is the most prevalent chronic inflammatory disease of the central

66 nervous system (CNS) in young adults (1). To date, the causes of MS are not fully understood,

67 yet it is presumed to be an autoimmune disease driven by autoreactive T cells targeting CNS

68 antigens (2). Upon reactivation at the CNS borders, autoreactive immune cells infiltrate the

69 CNS parenchyma and attack the myelin sheaths that surround neurons, eventually leading to

70 axonal loss and causing neuroinflammation (3,4).

71 Transmigration of T cells across the blood-brain barrier (BBB) represents a key step in the

72 pathology of MS and its animal model experimental autoimmune encephalomyelitis (EAE) (5),

73 which follows a multistep process involving interaction of different adhesion molecules with

74 integrins (6,7). While expression of these molecules on the BBB is usually low, pro-

75 inflammatory cytokine signaling during neuroinflammation induces dramatic brain

76 microvascular endothelial cell (BMEC) activation (8-12). IL-1 signaling is an essential pathway

77 driving the expression of adhesion molecules like intercellular adhesion molecule 1 (ICAM-1)

78 and vascular cell adhesion molecule 1 (VCAM-1) on BMECs through nuclear translocation of

79 nuclear factor 'kappa-light-chain-enhancer' of activated B cells (NF-κB), thus promoting the

80 firm adhesion of leukocytes to the BBB (13-18).

81

82 A20 is an integral molecule for the negative regulation of the NF-κB signaling pathway. The

83 transcription factor NF-κB is active in BMECs in a variety of conditions associated with vascular

84 dysfunction and BBB impairment (19-21). Moreover, a protective role was ascribed to the NF-

85 κB essential modulator (NEMO) and the upstream kinase TAK1 in BMECs, as their deletion

86 causes BBB disruption and BMEC cell death partly mediated by TNF signaling (22). Importantly,

87 A20 is well-known to counteract the cytotoxic effects of TNF (23-25).

88   Genetic variations in the *TNFAIP3* gene, encoding for A20, have been linked to the

89   susceptibility to MS (26). Interestingly, mice deficient for A20 develop a spontaneous

90   neuroinflammation with remarkable micro- and astrogliosis as well as BMEC activation (27).

91   Deletion of A20 specifically in astrocytes or microglia further proved the protective function

92   of A20 in the establishment of active EAE and spontaneous neuroinflammation (28-30).

93   Besides glial cells, also ECs express high levels of A20 in the steady state condition (31), yet

94   studies regarding the role of A20 in CNS-ECs are so far lacking.

95

96   We found that mice lacking A20 in CNS-ECs develop an exacerbated EAE disease upon

97   adoptive transfer (AT) of encephalitogenic T cells. While we did not observe pronounced

98   alterations in the structure of the microvasculature or BBB integrity, we found that loss of A20

99   in CNS-ECs dramatically upregulates ICAM-1, VCAM-1 and the Inducible T cell co-stimulator

100   ligand (ICOSL). Using a CNS-microvasculature endothelial cell-specific viral vector to silence

101   ICOSL, we could partly rescue the more severe AT-EAE course in A20$^{\Delta CNS-EC}$ mice and delay the

102   onset of an active EAE disease in wildtype mice. Mechanistically, we demonstrate that ICOSL

103   drives the adhesion of Th1 and Th17 cells to an in vitro BBB model. Taken together, our work

104   reveals A20-regulated ICOSL as an adhesion molecule involved in the multi-step

105   transmigration process of T cells across the BBB under inflammatory conditions.

106

107   RESULTS

108   *Mice with A20-deficient CNS-ECs are hypersensitive to adoptive transfer experimental*

109   *autoimmune encephalomyelitis*

110   To investigate the involvement of CNS-endothelial A20 in autoimmune neuroinflammation we

111   generated A20$^{\Delta CNS-EC}$ mice which lack A20 in CNS-ECs upon tamoxifen (TAM)-inducible Cre

112 recombination (Figure 1A). RT-PCR and Western blot analyses of primary mouse brain

113 microvascular endothelial cells (pMBMECs) confirmed the deletion of *Tnfaip3*/A20 (Figure 1B,

114 C). To our surprise, we did not observe a difference in disease severity between A20$^{\Delta CNS-EC}$

115 mice and littermate controls in three different active EAE models where mice were immunized

116 with MOG$_{35-55}$ in complete Freund's adjuvant (CFA) (Supplemental Figure 1A-L). As CFA is

117 known to activate CNS-ECs (13), we next studied the phenotype of A20$^{\Delta CNS-EC}$ mice in an

118 adoptive transfer (AT)-EAE model which circumvents CFA-driven effects.

119 Interestingly, we found that compared to littermate controls, the majority of A20$^{\Delta CNS-EC}$ mice

120 developed EAE symptoms (Figure 1D). This resulted in an increased average disease severity,

121 with increased area under the curve (AUC) values and maximum scores (Figure 1E-G). A20$^{\Delta CNS-EC}$

122 ^{EC} mice furthermore showed a tendency towards earlier disease onset (Figure 1H). To exclude

123 astrocytic contamination as previously reported for the Slco1c1-CreER^{T2} mouse line (32) we

124 generated mice lacking A20 in all endothelial cells (A20$^{\Delta EC}$) by crossing A20$^{fl/fl}$ mice to

125 Cdh5(PAC)-CreER^{T2} mice (33) to validate our data. Indeed, we observed a very similar

126 phenotype with an overall increased disease severity (Figure 1I-K). A20$^{\Delta EC}$ mice furthermore

127 showed a significantly accelerated disease onset, with mice developing symptoms in average

128 two days earlier than controls (Figure 1L).

129 We next focused on a different model involving CNS inflammation and used an MCAO model

130 to induce stroke in A20$^{\Delta CNS-EC}$ mice. We observed significantly increased infarct and edema

131 volumes, overall leading to a mildly increased edema-corrected infarct volume in A20$^{\Delta CNS-EC}$

132 mice (Supplemental Figure 2). Together, this data strongly suggests a protective role for CNS

133 EC-A20 in CNS autoimmunity and sterile inflammation.

134

135 *Loss of A20 in CNS-ECs drives immune cell infiltration into the CNS*

136   To investigate the extent of leukocyte infiltration, we isolated immune cells from the SC at the

137   peak of AT-EAE disease and analyzed cell subsets and cytokine production by flow cytometry

138   after antigen recall (Figure 2A). We found dramatically increased numbers of CD45.1$^+$

139   transferred and amongst them CD40L$^+$ MOG$_{35-55}$-specific T cells in A20$^{\Delta CNS-EC}$ mice (Figure 2B,

140   C). Also, the number of cytokine-producing cells was significantly increased (Figure 2D-F).

141   Furthermore, absolute cell counts of dendritic cells, neutrophils and monocytes were elevated

142   in A20$^{\Delta CNS-EC}$ mice (Supplemental Figure 3A-E). We next analyzed the location of CD3$^+$ T cells

143   in the SC by immunostaining. Compared to controls, we found high numbers of T cells in the

144   SC of A20$^{\Delta CNS-EC}$ mice, with cells forming perivascular cuffs but also penetrating deep into the

145   parenchyma (Figure 2G). As EAE disease severity is strongly dependent on the ratio of effector

146   to regulatory T cells (Treg cells) (34), we next assessed if loss of A20 in CNS-ECs influences Treg

147   cell frequencies. We did not observe changes in Treg cell frequencies or effector T cell to Treg

148   cell ratio at day post transfer (DPT) 18 (Supplemental Figure 4A-D). Based on these

149   observations, we conclude that the loss of A20 in CNS-ECs promotes immune cell infiltration

150   across the BBB under inflammatory conditions without affecting the proportion of effector T

151   cells to Treg cells.

152   We next addressed the question whether loss of A20 in CNS-ECs causes infiltration of immune

153   cells even in the absence of exogenously induced inflammation. We assessed the numbers of

154   CD45$^+$ total infiltrates, TCRβ$^+$ T cells and CD11b$^+$ myeloid cells in the steady state CNS one

155   week after TAM injection. Indeed, we found increased numbers of immune cells infiltrating

156   the CNS in A20$^{\Delta CNS-EC}$ mice in the steady state compared to littermate controls (Figure 2H-J,

157   Supplemental Figure 3F, G). Interestingly, the frequencies of TCRβ$^+$ T cells and CD11b$^+$ myeloid

158   cells amongst all infiltrating cells were not altered (Supplemental Figure 3H). Taken together,

159 this data suggests that the loss of A20 in CNS-ECs provokes the infiltration of immune cells

160 across the BBB even in the absence of an inflammatory stimulus.

161

162 *A20 protects from excessive adhesion molecule expression in steady state CNS-ECs*

163 To test whether deficiency for A20 in BMECs results in CNS blood vessel abnormalities, we

164 performed immunostainings of the endothelial cell marker CD31 and of collagen IV as an

165 integral basement membrane component. We neither observed alterations in vessel length

166 nor increased numbers of empty basement membrane strands, also known as string vessels

167 (35), in the brains of A20$^{\Delta CNS-EC}$ mice (Figure 3A, B). We next focused on BBB integrity in

168 A20$^{\Delta CNS-EC}$ mice. By performing immunostaining for the tight junction molecule occludin, we

169 observed reduced fluorescence intensity in BMECs of A20$^{\Delta CNS-EC}$ mice (Figure 3E, F). However,

170 brain weight, as an indicator of brain edema, was not increased compared to controls (Figure

171 3D). To exclude a disruption of the BBB and the blood-spinal cord barrier (BSCB), we assessed

172 the integrity by injecting a small 3-5 kDa dextran tracer and measuring fluorescence in brain

173 or SC. Compared to mice at the peak of an active EAE disease, in which BBB and BSCB integrity

174 are compromised, A20$^{\Delta CNS-EC}$ mice did not show an increased permeability for FITC-dextran,

175 confirming normal BBB and BSCB integrities (Figure 3G, H).

176 As T cell transmigration across the BBB is mainly dependent on the surface expression levels

177 of adhesion molecules (36), we next investigated if the increased numbers of immune cells

178 infiltrating the CNS in A20$^{\Delta CNS-EC}$ mice were due to alterations in adhesion molecule expression.

179 By performing immunostaining of VCAM-1 together with collagen IV, we detected

180 dramatically increased numbers of VCAM-1^{+} microvessels in the brain cortex of A20$^{\Delta CNS-EC}$ mice

181 (Figure 4A, B). Also, ICAM-1 levels were dramatically increased on CNS microvessels in A20$^{\Delta CNS-}$

182 ^{EC} mice, with almost 100% of CNS-ECs expressing ICAM-1 (Figure 4C-F). Both molecules are

183   well-known to mediate the multistep process of immune cell transmigration across the BBB

184   (6). Our data suggests that loss of A20 in CNS-ECs does not influence BBB integrity but causes

185   a dramatic upregulation of cell adhesion molecules, which at least partially drives leukocyte

186   infiltration and AT-EAE severity.

187

188   *RNA-seq reveals strong activation of CNS-ECs in A20$^{\Delta CNS-EC}$ mice*

189   Blocking immune cell infiltration by targeting α4-integrin, a binding partner of VCAM-1, with

190   natalizumab is an effective treatment option for MS patients presenting with a relapsing-

191   remitting disease course (37-39). Yet, this therapeutic strategy comes with a risk to develop

192   severe CNS infections (40). Identification of novel adhesion molecules facilitating the

193   extravasation of specific cell subsets is thus essential. We therefore made use of the A20$^{\Delta CNS-}$

194   ^{EC} mice to characterize their CNS-EC adhesion molecule profile in-depth by RNA sequencing.

195   Crossing these mice to R26R-EYFP reporter mice allowed us to sort for CNS-ECs from the SC

196   with Cre-mediated recombination, which could be observed in approximately 90% of all ECs

197   (Supplemental Figure 5A, B). To focus on molecules involved in immune cell transmigration,

198   we included a control group of wildtype-like A20$^{fl/fl}$ mice at day post immunization (DPI) 10 of

199   an active EAE disease, a timepoint where immune cell extravasation across the BBB is known

200   to happen (41). We first confirmed the purity of the sorted SC-ECs by plotting endothelial

201   marker genes as well as genes specific for other CNS-resident cells (Figure 5A). We next

202   focused on genes that were differentially expressed (DE) in either the A20$^{\Delta CNS-EC}$-eYFP or the

203   EAE group compared to the control condition, respectively. While most of the DE genes were

204   found in the EAE situation, a substantial amount of DE genes could also be identified in

205   A20$^{\Delta CNS-EC}$-eYFP mice (Figure 5B). The overlap of DE genes in the A20$^{\Delta CNS-EC}$-eYFP and the EAE

206   condition resulted in 26 genes that were commonly upregulated and 4 genes that were

207 commonly downregulated (Figure 5C, D). Amongst these genes, *Icam1* and *Vcam1*

208 represented the top upregulated genes, confirming our previous findings. Also, *Tnfaip3* itself

209 was among the upregulated genes, yet mapping the reads of *Tnfaip3* to the genetic locus

210 confirmed the excision of exon 3 in A20$^{\Delta CNS-EC}$ mice, rendering the transcript non-translatable

211 (Supplemental Figure 5C) (42). To investigate if other genes related to immune cell

212 transmigration across the BBB were amongst the commonly DE genes, we performed a KEGG

213 pathway analysis. The most prominent pathways were the inflammatory *NF-κB* and *TNF*

214 *signaling pathways*, pointing out the essential function of A20 as negative regulator of these

215 signaling cascades. Interestingly, and as hypothesized, also the *Cell adhesion molecules*

216 pathway was amongst the top KEGG terms (Figure 5E). This was further underscored by a

217 Gene Ontology (GO) term analysis, in which *Leukocyte cell-cell adhesion*, *Membrane to*

218 *membrane docking* and *Cell adhesion* represented the top affected Biological Processes

219 (Suppl. Figure 5D).

220

221 *ICOSL is upregulated on CNS-ECs under inflammatory conditions*

222 Interestingly, besides *Icam1* and *Vcam1* also *Icosl* was identified as cell adhesion molecule in

223 the KEGG pathway analysis and moreover, *Icosl* expression levels in A20$^{\Delta CNS-ECs}$ and DPI10 ECs

224 were very similar to those of *Icam1* and *Vcam1* (Supplemental Figure 5E). RT-PCR validation

225 of *Icosl* expression indeed confirmed its upregulation in sorted CNS-ECs from naïve A20$^{\Delta CNS-EC}$

226 mice compared to littermate controls (Supplemental Figure 5F). In addition, we could validate

227 the upregulation of ICOSL protein on CNS-ECs in vivo during EAE (Figure 5F, G).

228

229 Expression of ICOSL on peripheral ECs as well as on the human BMEC-derived cell line

230 hCMEC/D3 is strongly upregulated by various inflammatory stimuli in vitro (43,44). We thus

231 investigated *Icosl* mRNA levels in pMBMECs isolated from A20$^{\Delta CNS-EC}$ mice and found increased

232 levels in response to TNF stimulation compared to unstimulated or TNF-stimulated A20$^{fl/fl}$

233 control pMBMECs (Supplemental Figure 5G). Furthermore, while TNF stimulation of wildtype

234 pMBMECs significantly increases *Icosl* expression, IL-1β stimulation led to an even higher

235 upregulation of *Icosl* mRNA levels (Supplemental Figure 5H). Moreover, ICOSL upregulation in

236 response to IL-1β stimulation followed a very similar pattern like ICAM-1 and VCAM-1

237 (Supplemental Figure 5I). These data indicate that in addition to ICAM-1 and VCAM-1, also

238 ICOSL is upregulated on CNS-ECs under inflammatory conditions and may therefore contribute

239 to the onset of neuroinflammation.

240

241 *Silencing of CNS microvascular EC-ICOSL ameliorates AT-EAE in A20$^{\Delta CNS-EC}$ mice*

242 To evaluate the function of CNS EC-ICOSL in autoimmune neuroinflammation, we knocked

243 down ICOSL by delivering shRNA to CNS microvascular ECs using the AAV-BR1. As not 100% of

244 CNS microvascular ECs are transduced upon AAV-BR1 application (45), we first confirmed that

245 the location of the transduced ECs was in close proximity to the infiltrating immune cells

246 during EAE. Indeed, we found multiple GFP$^+$ vessels in close proximity to CD3$^+$ T cells in the

247 perivascular space, but also in close proximity to T cells infiltrating into the SC parenchyma in

248 EAE mice treated with AAV-BR1-eGFP (Figure 6A, B). Immunofluorescence furthermore

249 proved specificity of the AAV-BR1-eGFP in targeting vessels, as eGFP only co-localized with

250 laminin but not cortical neuronal NeuN (Supplemental Figure 6A). Next, we designed a CNS

251 microvascular EC-specific AAV carrying either an shRNA against *Icosl* (AAV-BR1-shIcosl) or a

252 scrambled shRNA (AAV-BR1-con) (Figure 6C). Both constructs express a GFP reporter under

253 the relatively weak RSV promoter, which was chosen to exclude potential GFP-induced

254 cytotoxicity (46). Yet, GFP intensity was still strong enough to validate the target specificity.

255 Upon injection of the AAV-BR1-shIcosl construct, GFP$^+$ cells could only be found among the

256 CD31$^+$ Ly6C$^+$ EC population, but not in other CNS-resident cells (Supplemental Figure 6B-F).

257 Transduction of pMBMECs with AAV-BR1-shIcosl furthermore proved the efficiency of this

258 virus to knockdown *Icosl* as expression levels were reduced by approximately 70% in IL-1β

259 stimulated pMBMECs (Supplemental Fig 6G). Flow cytometry of CNS-ECs upon in vivo

260 administration of AAV-BR1-shIcosl furthermore demonstrated a significant reduction in the

261 mean fluorescence intensity of ICOSL as well as in the percentage of ICOSL$^+$ ECs in mice after

262 immunization with MOG$_{35-55}$/CFA (Figure 6D, E). Of note, treatment with AAV-BR1-shIcosl did

263 not influence protein levels of ICAM-1 or VCAM-1 in CNS-ECs (Supplemental Figure 6H, I).

264

265 We next used this system to knockdown ICOSL in CNS microvascular ECs in A20$^{\Delta CNS-EC}$ mice to

266 evaluate the contribution of ICOSL to their increased EAE phenotype. Administration of AAV-

267 BR1-shIcosl, but not AAV-BR1-con, mildly ameliorated the AT-EAE disease course including the

268 area under the curve, the day of onset and the score at DPT7, a timepoint shortly after disease

269 onset (Figure 6F-I). Furthermore, AAV-BR1-shIcosl administration significantly reduced the

270 number of transferred CD45.1$^+$ T cells infiltrating into the SC (Figure 6J). Thus, ICOSL

271 participates in driving autoimmune neuroinflammation in A20$^{\Delta CNS-EC}$ mice and its knockdown

272 reduces the infiltration of encephalitogenic cells into the CNS.

273

274 *Endothelial ICOSL influences day of active EAE onset in wildtype mice*

275 Next, we wanted to recapitulate our findings in wildtype mice in an active EAE model. For this,

276 AAV-BR1-shIcosl was injected i.v. and two weeks later mice were immunized with MOG$_{35-55}$ in

277 CFA. Confirming our previous findings, we also detected a mildly ameliorated disease and a

278 tendency towards reduced numbers of infiltrating immune cells in mice treated with AAV-

279 BR1-shIcosl (Figure 6K-O). More importantly, disease onset could be delayed by an average of

280 two days in the AAV-BR1-shIcosl treated group (Figure 6M). These findings confirm a

281 functional role for CNS microvascular EC-ICOSL in driving autoimmune neuroinflammation,

282 possibly by promoting the infiltration of pathogenic T cells.

283

284 *ICOSL promotes T-cell adhesion to the BBB in vitro*

285 ICOSL is an immunoglobulin superfamily member, expressing immunoglobulin-like domains

286 that are known to mediate cell-cell adhesion through binding in a homophilic or heterophilic

287 manner (47). ICOSL thus shares structural similarities with the known adhesion molecules

288 ICAM-1, VCAM-1 and the more recently characterized molecules activated leukocyte adhesion

289 molecule (ALCAM-1), melanoma cell adhesion molecule (MCAM-1) and dual immunoglobulin-

290 domain containing cell adhesion molecule (DICAM-1) (48-52). Recently, it was shown that

291 ICOSL can bind to $\alpha_V\beta_3$, an integrin known to be important for EAE development by mediating

292 the recruitment of encephalitogenic T cells to the CNS (53,54). This body of evidence led us to

293 hypothesize that CNS EC-ICOSL could be involved in mediating immune cell adhesion to the

294 BBB. To prove this, we performed T cell migration assays as well as static T cell adhesion assays

295 on anti-ICOSL-treated pMBMECs. We found significantly reduced numbers of adhering MOG_{35-55}-specific Th1 and Th17 cells under static conditions when ICOSL was blocked on IL-1β-

297 stimulated pMBMECs (Figure 7A-C). We next assessed the post-arrest behavior of Th1 cells

298 under physiological flow conditions. The numbers of arrested T cells showed a trend towards

299 lower numbers of cells arresting when ICOSL was blocked, however, due to the variance across

300 the individual experiments not reaching statistical significance (Figure 7D). The post-arrest

301 behavior, which we categorized into fractions of T cells that were detaching, probing, probing

302 followed by diapedesis, crawling and crawling followed by diapedesis, was unaltered when

14

303 ICOSL was blocked (Figure 7E). Also, the crawling distance and crawling speed of the T cells

304 that successfully performed diapedesis following crawling on the pMBMECs was not changed

305 (Figure 7F, G). Taken together, ICOSL promotes the arrest of Th1 and Th17 cells to the

306 monolayer without influencing the post-arrest behavior of T cells on pMBMECs under

307 physiological flow.

308

309 DISCUSSION

310 In this study, we identified a previously unknown role of CNS-EC A20 in neuroinflammation.

311 Our results show that the loss of A20 in CNS-ECs strongly increased the risk to develop EAE

312 upon transfer of encephalitogenic T cells into naïve recipients and accelerates disease onset.

313 ECs lacking A20 were dramatically activated which resulted in the upregulation of cell

314 adhesion molecules like ICAM-1 and VCAM-1 but also ICOSL. We propose here that A20 serves

315 as a gatekeeper for the activation of ECs, and its absence drives transmigration of

316 encephalitogenic T cells across the BBB and by this, at least partially, contributes to the

317 increased disease susceptibility.

318 Supporting evidence for this hypothesis comes from the observation that innate immune

319 activation, for example mediated by CFA used in the active EAE induction protocol, drives

320 endothelial activation and promotes upregulation of adhesion molecules already before onset

321 of disease, suggesting a causal role for endothelial activation in disease initiation (13,55,56).

322 Interestingly, and in contrast to A20-deficiency in microglia and astrocytes (28,29), we did not

323 observe alterations in an actively induced EAE disease in mice with A20-deficient ECs. It seems

324 likely that the endothelial activation in response to CFA in the active EAE model masks the

325 effects driven by A20 deletion in CNS-ECs and could thus explain the difference seen in AT-

326 EAE but not active EAE outcomes.

327

328 We observed an increased infiltration of immune cells into the CNS of A20$^{\Delta CNS-EC}$ mice in steady

329 state and after AT-EAE. To enter the CNS, immune cells need to cross the BBB, which

330 represents a key step in the pathology of CNS autoimmune diseases such as MS. Both immune

331 cells and BMECs require a certain state of activation to allow immune cells to cross the BBB.

332 The influence of cytokines and other inflammatory mediators secreted by activated T cells but

333 also innate immune cells on the endothelium has been extensively described (57-59). In

334 particular, pro-inflammatory cytokines like TNF or IL-1β that activate the NF-κB pathway are

335 essential in mediating the upregulation of cell adhesion molecules on BMECs which promote

336 the infiltration of pathogenic T cells and the development of CNS autoimmunity (13,60,61).

337 Upregulation of ICAM-1 and VCAM-1 in CNS-ECs has been described in A20$^{-/-}$ mice in the

338 steady-state, however, it was suggested that this upregulation of adhesion molecules was due

339 to the overall heightened cerebral inflammation present in A20$^{-/-}$ mice (27). Opposingly, we

340 show here that ICAM-1 and VCAM-1 upregulation in steady-state CNS-ECs was driven by an

341 endothelial-intrinsic response to A20-deficiency, as A20$^{\Delta CNS-EC}$ mice manifested a strong

342 expression of both molecules without external inflammatory stimulation.

343 Our results furthermore indicate that rather excessive adhesion molecule expression and not

344 BBB breakdown are responsible for the pronounced CNS immune cell infiltration in A20$^{\Delta CNS-EC}$

345 mice. It was earlier proposed that NF-κB signaling in BMECs is essential for maintaining barrier

346 integrity (22). Disruption of NF-κB signaling through CNS EC-specific deletion of NEMO or TAK1

347 resulted in an increased BBB permeability which was suggested to result from impaired A20-

348 mediated occludin stabilization (22). Although we could confirm that A20-deficiency in CNS-

349 ECs leads to decreased occludin levels, this reduction did not cause BBB or BSCB breakdown

350 in our study, underscoring the debate about the necessity of occludin for barrier integrity (62-

351 65). Our data furthermore corroborates earlier reports of A20$^{-/-}$ and A20$^{+/-}$ mice, which also

352 did not manifest any signs of BBB disruption (27,66). We can thus conclude that activation of

353 BMECs through loss of A20 provokes expression of cell adhesion molecules which promotes

354 the firm adhesion of immune cells to the BBB and facilitates their entry into the CNS.

355 Supporting our findings, we furthermore found a more severe disease pathology in the MCAO

356 model, a model involving sterile CNS inflammation, in A20$^{\Delta CNS-EC}$ mice. Interestingly, T cells

357 infiltrate into the injured areas as early as 24h post MCAO induction (67) and blocking of the

358 α4-integrin unit of VLA-4, the binding partner of VCAM-1, reduces the infarct volumes by

359 restricting CNS T cell infiltration (68,69). It is thus possible, that the increased infarct areas in

360 A20$^{\Delta CNS-EC}$ arise from a more pronounced T cell infiltration due to the massive EC activation.

361

362 The success of targeting the VLA-4 subunit α4-integrin with natalizumab in MS therapy points

363 out the attractiveness of interfering with transmigration of immune cells across the BBB in

364 diseases involving CNS inflammation. Yet, due to the potential side effects of this treatment

365 strategy it is necessary to identify alternative targets for therapeutic intervention. In recent

366 years, alternative cell adhesion molecules involved in immune cell transmigration across the

367 BBB have been identified. ALCAM was found to be an important adhesion molecule guiding B

368 cell and monocyte trafficking across the BBB, yet deletion of this molecule dramatically

369 influences the barrier integrity and causes more severe EAE disease (48,49,70). Also, MCAM

370 was implicated in several studies to be essential for CD8^{+} as well as Th17 cell migration across

371 the BBB (50,51,71). More recently, also DICAM was found to be involved in Th17 cell migration

372 across the BBB and was suggested as a potential target in progressive MS forms (52). While

373 progress has been made in recent years, the spectrum of molecular interactions occurring at

374 the CNS-peripheral interface is certainly not yet disentangled in its entirety. We here identified

375   A20-regulated ICOSL as adhesion molecule contributing to the firm adhesion of $MOG_{35\text{-}55}$

376   specific pro-inflammatory Th1 and Th17 cells to the BBB. Although the reduction in T cell

377   adhesion when ICOSL was blocked appears rather mild, the effect is in line with studies

378   investigating T cell adhesion to other adhesion molecules (52,72). ICOSL was only recently

379   reported to mediate adhesion of podocytes by binding to the $\alpha_V\beta_3$ integrin through its RGD

380   motif (54). Interestingly, Roussel *et al.* earlier introduced a human mutation in ICOSL, which

381   was found in one patient with a combined immunodeficiency syndrome (73). The authors

382   identified an involvement of endothelial ICOSL in mediating the transmigration of T cells and

383   neutrophils across an in vitro endothelial barrier (73). We here corroborate these findings and

384   extent the involvement of endothelial ICOSL in immune cell adhesion from the periphery to

385   brain-derived pMBMECs. Future studies are, however, necessary to determine the exact

386   binding partner of ICOSL that mediates this adhesion and to further characterize the spectrum

387   of immune cells having the capacity to bind to ICOSL.

388

389   We could furthermore underscore the functional role of CNS EC-ICOSL in the development of

390   autoimmune neuroinflammation by in vivo silencing of ICOSL with a CNS-microvascular

391   endothelial specific AAV. Although the GFP signal from our AAV-BR1-shIcosl likely

392   underrepresents the percentage of transduced cells due to the comparably weak RSV

393   promoter driving GFP expression, we could confirm the efficiency of our construct to knock

394   down ICOSL specifically in CNS-ECs both in vitro and in vivo. More importantly, we were able

395   to partly rescue the accelerated disease outcome in $A20^{\Delta CNS\text{-}EC}$ mice by treating them with

396   AAV-BR1-shIcosl, although not reaching statistical significance. Notably, and opposed to

397   observations from Roussel *et al.*, protein levels of ICAM-1 and VCAM-1 molecules were not

398   affected by silencing of ICOSL (73). The high levels of these molecules remaining in $A20^{\Delta CNS\text{-}EC}$

399   mice might explain the rather mild amelioration in the day of disease onset and the overall

400   disease severity upon treatment with AAV-BR1-shIcosl. Nevertheless, silencing of ICOSL on

401   CNS-ECs restricted the infiltration of transferred encephalitogenic T cells into the CNS of

402   A20$^{\Delta CNS-EC}$ mice, confirming its contribution to T-cell mediated autoimmunity.

403

404   In agreement with these observations, our results additionally showed that the day of active

405   EAE onset could be delayed when ICOSL was knocked down in CNS-ECs of wildtype mice. As

406   transmigration of immune cells through the BBB precedes the development of EAE symptoms

407   (74,75), our data suggests that the delayed disease development is due to an impairment of T

408   cell adhesion to the BBB. The phenotype we observed is in accordance with EAE data from

409   mice in which other cell adhesion molecules (ICAM-1, ICAM-2, VCAM-1) were targeted

410   (36,76). Targeting of CNS microvascular EC-ICOSL thus seems to be an attractive approach for

411   controlling infiltration of pathogenic immune cells in the context of autoimmune

412   neuroinflammation. However, ICOSL is well-known to also function as co-stimulatory

413   molecule in an immunological context (77-79) and earlier studies targeting ICOS indicated a

414   protective effect of ICOS-ICOSL interaction in the priming phase of EAE (80,81). Thus, anti-

415   ICOSL treatment for CNS autoimmunity needs to be carefully evaluated as the desired effect

416   strongly relies on cell specificity as well as the time point of therapy.

417

418   In conclusion, our study sheds new light on two important aspects in the pathology of CNS

419   inflammation. Firstly, our data demonstrates a protective role for CNS endothelial A20 by

420   preventing the excessive expression of cell adhesion molecules and thus regulating the

421   infiltration of immune cells into the CNS. Secondly, we discovered ICOSL as an A20-regulated

422   cell adhesion molecule mediating the firm adhesion of Th1 and Th17 cells to the BBB. Overall,

423   this study suggests ICOSL as a potential therapeutic target in the treatment of CNS

424   autoimmune diseases such as MS.

425

426   METHODS

427   *Mice*

428   All mice used were on the C57BL/6 background and housed under specific pathogen-free

429   conditions. A20$^{fl/fl}$ mice (82) were crossed to Slco1c1-CreER^{T2} mice (32) (A20$^{\Delta CNS-EC}$) and used

430   for A20 western blot analysis, immunofluorescent stainings of brain vessels with collagen IV,

431   CD31, occludin and VCAM-1, MCAO and active EAE in facility 2. For all other experiments

432   analyzing A20$^{\Delta CNS-EC}$ mice, A20$^{fl/fl}$ mice (42) were crossed to Slco1c1-CreER^{T2} mice (32). For

433   generation of A20$^{\Delta EC}$ mice, A20$^{fl/fl}$ mice (42) were crossed to Cdh5(PAC)-CreER^{T2} (33) mice. Cre-

434   negative A20$^{fl/fl}$ littermates were used as controls. For sequencing experiments, A20$^{\Delta CNS-EC}$

435   mice were crossed to R26R-EYFP reporter mice (83). For AT-EAE experiments, Ly5.1 mice

436   (B6.SJL-PtprcaPepcb/BoyCrl) were used as donor mice.

437

438   *Tamoxifen treatment*

439   A 20 mg/ml tamoxifen (Sigma-Aldrich) solution was prepared by suspension in olive oil (Sigma-

440   Aldrich) containing 5 % ethanol. Tamoxifen was dissolved by rotation overnight at 4°C. Mice

441   were injected intraperitoneally (i.p.) with 100 µl (= 2 mg tamoxifen) at five (for Slco1c1-CreER^{T2}

442   strains) or three (for Cdh5(PAC)-CreER^{T2} strains) consecutive days at the age of 6-7 weeks and

443   mice were used for experiments 2-4 weeks thereafter, unless otherwise indicated. A20$^{fl/fl}$

444   littermate controls were treated equally.

445

446   *Active EAE induction*

447 An emulsion of MOG$_{35-55}$ in CFA was prepared by mixing 1 mg/ml MOG$_{35-55}$ (GenScript) in PBS

448 with Complete Freund's Adjuvants (CFA, BD Biosciences) supplemented with *mycobacterium*

449 *tuberculosis* H37RA (BD Biosciences). 50 μg MOG$_{35-55}$/CFA were injected subcutaneously into

450 the tail base. At the day of immunization and two days later, 150 ng pertussis toxin (PTx, List

451 Biological Laboratories) in PBS were applied i.p. unless otherwise stated. For active EAE

452 induction in facility 2 (Supplemental Figure 1E-H) mice were immunized with an immunizing

453 emulsion (EK-2110, Hooke Laboratories) containing a MOG$_{35-55}$ peptide in Freund's adjuvant

454 as described before (84). Additionally, mice were treated with 400 ng PTx i.p. on the day of

455 immunization and one day later.

456 Mice were weighed daily and clinical scores were documented as follows: 0, no disease; 0.5:

457 limb tail; 1: paralyzed tail; 1.5: weakened righting reflex; 2: no righting reflex; 3: partial

458 paralysis of hind legs; 3.5: paralysis of one hind leg; 4: paralysis of both hind legs.

459

460 *Adoptive transfer (AT) EAE induction*

461 Ly5.1 mice were immunized with MOG/CFA and PTx as described above. Ten days after

462 immunization, spleen, inguinal and paraaortic lymph nodes were harvested and single-cell

463 suspensions were prepared and cultured in vitro in the presence of MOG$_{35-55}$ peptide (20

464 μg/ml), anti-IFNγ (10 μg/ml; BioXCell), and IL-23 (15 ng/ml; Miltenyi Biotec). After 4 days, cells

465 were harvested and examined for blasting lymphocytes, as based on forward and side scatter

466 properties in flow cytometry. Cell suspensions were adjusted to 50×10^6 blasting cells/ml, and

467 100 μl of this suspension was injected intravenously (i.v.) into the tail veins of recipient mice,

468 accompanied by i.p. injections of PTx (150 ng) at the same day and 2 days later. Mice were

469 weighed daily and the clinical scores were assessed according to the scoring system described

470 above.

471

Permanent occlusion of the middle cerebral artery (MCAO)

473 The ischemic stroke model was performed as described before (85). Briefly, mice were

474 anaesthetized using tribromoethanol (2.5%, 15µl/g body weight, i.p.). After a skin incision and

475 removal of the left temporal muscle, a burr hole was drilled through which the stem of the

476 middle cerebral artery was occluded by electrocoagulation (Model ICC50, Erbe). After

477 suturing, mice were placed under a heating lamp until they fully recovered. After 48h, mice

478 were perfused intracardially under deep anesthesia and brains were removed. Coronal

479 cryosections were cut every 400 µm and stained using a silver technique (86). Infarcted areas

480 were measured using ImageJ and infarct volume, edema, and edema-corrected infarct volume

481 were calculated as described before (86).

482

Immunofluorescence staining

484 Immunoflurescence stainings were performed on fixed frozen sections of 10-20 µm. Primary

485 antibodies against CD3ε (145-2C11, Armenian hamster monoclonal, eBioscience™, Thermo

486 Fisher Scientific, 1:100), NeuN (1B7, Mouse monoclonal, Invitrogen Thermo Fisher Scientific,

487 1:500), CD31 (rabbit polyclonal, abcam, 1:100 or MEC 13.3, rat monoclonal, BD Pharmingen™,

488 1:500), laminin 1+2 (rabbit polyclonal, abcam, 1:500), collagen IV (rabbit polyclonal, abcam,

489 1:1000), occludin (rabbit polyclonal, Proteintech, 1:1000) and VCAM-1 (MVCAM.A, rat

490 monoclonal, BD Pharmingen™, 1:1000) were incubated over night at 4°C. Sections were

491 washed and secondary antibodies against rabbit IgG (CF488A, Sigma-Aldrich, 1:800 or CF™

492 555, Sigma-Aldrich, 1:800 or Cy3, Jackson ImmunoResearch Labs, 1:400), Armenian hamster

493 (Alexa Fluor 647, Jackson ImmunoResearch Labs, 1:800), mouse IgG (CF™ 647, Sigma-Aldrich,

494 1:500) or rat IgG (Alexa 488, Thermo Fisher Scientific, 1:400) were added for 45 min - 1.5 h at

495 room temperature. Afterwards, sections were mounted with DAPI Fluoromount-G® Mounting

496 Medium (SouthernBiotech) or Mowiol 4-88 (Carl Roth) and images were acquired at a TCS SP8

497 inverse confocal microscope (Leica) or a DMI 6000B fluorescence microscope (Leica). Images

498 were analyzed with ImageJ software as described before (22).

499

500 *Culture of primary murine brain microvascular endothelial cells (pMBMEC)*

501 Cortices from 8-12-week-old wildtype mice were used for pMBMEC isolation as described

502 previously (87). Cells were seeded on 48-well culture dishes coated with Matrigel (ECM Gel

503 from Engelbreth-Holm-Swarm murine sarcoma, supplied by Sigma-Aldrich). Culture medium

504 was supplemented with 20% FCS, 2% non-essential amino acids and 5 µg/ml gentamicin. 1

505 ng/ml human fibroblast growth factor (FGF) (Sigma-Aldrich) and 4 µg/ml puromycin (Gibco)

506 were added for the first 48 h of culture. Afterwards, the medium was changed to puromycin-

507 free medium supplemented with FGF and was changed every other day.

508

509 *Leukocyte cell isolation from CNS for flow cytometry*

510 CNS tissue was dissected from mice transcardially perfused with 0.9% NaCl solution (Sigma-

511 Aldrich) and digested with 2 mg/ml collagenase II (Gibco) and 25 µg/ml DNase I (Roche) for 20

512 min at 37 °C and subsequently homogenized with a 18-G needle. Cells were then separated

513 using a 70–37–30% Percoll (Sigma-Aldrich) gradient centrifugation for 40 min, 500×g at 16 °C.

514 Cells at the 70/37% interphase were carefully collected and washed in PBS/FCS prior to 10 min

515 centrifugation at 500×g. To characterize MOG-specific T cells and cytokine production, cells

516 were plated in 96-well U-bottom plates and re-activated with 20 µg/ml MOG$_{35-55}$ peptide in

517 the presence of brefeldin A (Sigma-Aldrich) in T cell medium for 6 h at 37 °C. Afterwards, cells

518 were harvested and stained for flow cytometry analysis.

519

Endothelial cell isolation for flow cytometry

521 For CNS EC-isolation, mice were sacrificed and transcardially perfused as described above. The

522 dissected CNS tissue was digested with 2 mg/ml papain (Sigma-Aldrich) solution containing 25

523 μg/ml DNase I (Roche) for 30 min at 37 °C. During incubation, tissue was mechanically

524 homogenized using the gentleMACS™ Dissociator (Miltenyi). The resulting cell suspension was

525 filtered through a 70 μm cell strainer and centrifuged with a 22 % Percoll gradient for 30 min,

526 300×*g* at 15 °C. The pellet was used for flow cytometry staining.

527

Flow cytometry analysis

529 Before antibody staining, Fc receptors were blocked for 20 min using Fc-block (5 μg/ml)

530 (BioXCell). Single cell suspensions were stained for 30 min at 4 °C with antibodies against CD4

531 PerCP (GK1.5, rat monoclonal, 1:500, BioLegend), CD45 BV510 (30-F11, rat monoclonal, 1:200,

532 BioLegend), CD45.1 FITC (A20, mouse monoclonal, 1:1000, BioLegend), CD11b PECy7 (M1/70,

533 rat monoclonal, 1:1000, eBioscience™), Ly6C V450 (AL-21, rat monoclonal, 1:300 BD

534 Bioscience), Ly6C PerCP (HK1.4, rat monoclonal, 1:100, BioLegend), Ly6G PE (1A8, rat

535 monoclonal, 1:1000, BioLegend), CD11c APC (HL3, rat monoclonal, 1:800 BD Bioscience), CD19

536 PerCP (6D5, rat monoclonal, 1:400, BioLegend), TCRβ APC (H57-597, rat monoclonal, 1:1000,

537 BioLegend), CD31 PE (MEC 13.3, rat monoclonal, 1:100, BioLegend), CD31 PerCP-Cy5.5 (390,

538 rat monoclonal, 1:100, BioLegend), ICAM-1 APC (YN1/1.7.4, rat monoclonal, 1:300,

539 BioLegend), VCAM-1 PE-Cy7 (429 (MVCAM.A), rat monoclonal, 1:500, BioLegend), ICOSL

540 (CD275) PE (HK5.3, rat monoclonal, 1:100, BioLegend).

541 Afterwards, where indicated, cells were fixed and permeabilized with Cytofix/Cytoperm (BD

542 Bioscience) or Foxp3/Transcription Factor Staining Buffer Set (eBioscience™) and stained

24

543　overnight at 4 °C with intracellular antibodies. To specifically gate on MOG-specific cells, cells

544　were stained with anti-CD154 (CD40L) APC (MR1, hamster monoclonal, 1:200, BioLegend) and

545　cytokine production was assessed by staining with IL-17A eFl450 (eBio17B7, rat monoclonal,

546　1:300, eBioscience^{TM}), IFN-y PE-Cy7 (XMG1.2, rat monoclonal, 1:1000, eBioscience^{TM}) and

547　GM-CSF PE (MP1-22E9, rat monoclonal, 1:200, eBioscience^{TM}). Staining for Foxp3 was

548　performed with Foxp3-FITC (FJK-16s, rat monoclonal, 1:200, eBioscience^{TM}).

549　Cells were acquired with a FACSCanto II cytometer (BD Bioscience) using FACS Diva software

550　(BD Bioscience). Flow cytometry data was analyzed with FlowJo^{TM} software version 10 (BD

551　Bioscience). For all analyses, doublets (FSC and SSC properties) and dead cells (dye inclusion,

552　fixable viability dye APC-ef780 eBioscience^{TM}) were excluded.

553

554　*Fluorescence activated cell sorting (FACS) of CNS-ECs*

555　Endothelial cells from the spinal cord were isolated and subsequently stained with a surface

556　marker antibody panel and directly acquired at a FACSAria III (BD Bioscience) with a 100 μm

557　nozzle.

558

559　*RNA isolation and RNA sequencing*

560　For RNA sequencing 500 cells were sorted into lysis buffer and full-length cDNA was

561　synthesized using the SMART-Seq® v4 Ultra® Low Input Kit (Takarabio). 1 ng of the resulting

562　cDNA was used for library preparation (Illumina Nextera XT DNA Library Prep Kit) according to

563　the manufacturer's instructions. Quantity was assessed using Invitrogen's Qubit HS assay kit

564　and library size was determined using Agilent's 2100 Bioanalyzer HS DNA assay. Barcoded

565　RNA-Seq libraries were onboard clustered using HiSeq® Rapid SR Cluster Kit v2 using 8pM and

566　59bps and were sequenced on the Illumina HiSeq2500 using HiSeq® Rapid SBS Kit v2 (59 Cycle).

567 The raw output data of the HiSeq was preprocessed according to the Illumina standard

568 protocol.

569

570 *RNA sequencing data analysis*

571 Quality control on the sequencing data was performed with the FastQC tool (version 0.11.8,

572 https://www.bioinformatics.babraham.ac.uk/projects/fastqc/). RNA sequencing reads were

573 aligned to the ENSEMBL Mus_musculus.GRCm38 reference genome. The corresponding

574 annotation (ENSEMBL v76) was retrieved from ENSEMBL FTP website. The STAR aligner

575 (version 2.6.1a) was used to perform mapping to the reference genome.   Alignments were

576 processed with the featureCounts function of the Rsubread package (version 2.10.0), using

577 the annotation file also used for supporting the alignment. The exploration, modeling, and

578 interpretation of the expression data followed the protocols defined by Ludt *et. al* (2022) (88).

579 Exploratory data analysis was performed with the pcaExplorer package (version 2.22.0).

580 Differential expression analysis was performed with DESeq2 package (version 1.36.0), setting

581 the false discovery rate (FDR) cutoff to 0.05. Accurate estimation of the effect sizes (described

582 as log2 fold change) was performed using the apeglm shrinkage estimator (version 1.18.0).

583 Gene expression profiles were plotted as heatmaps (color-coded standardized z-scores for the

584 expression values, after regularized logarithm transformation) to enable comparison across

585 samples, created with the GeneTonic package (version 2.0.3) (89). For functional annotation

586 of Gene Ontology (GO) and analysis of KEGG pathway enrichment, the web-based DAVID 2021

587 tool was used.

588

589 *FITC-dextran permeability assay*

26

590 FITC-dextran (avg. mol. weight 3,000-5,000 Da, Sigma-Aldrich) was dissolved at 2 mM in PBS.

591 100 μl of this stock solution was injected i.p. into the mice. After 15 min, mice were sacrificed

592 and perfused with 0.9% NaCl solution. Spinal cords and half brains were weighed and

593 subsequently homogenized in 200 μl (spinal cord) or 500 μl (half brain) PBS in metal bead

594 lysing matrix tubes (MP Biomedicals) using the FastPrep-24™ (MP Biomedicals) system. Tubes

595 were centrifuged at 15,000 x g for 20 min at 4°C and 100 μl of the supernatant were

596 transferred into a 96 well flat black plate (Greiner). FITC fluorescence was measured with a

597 Spark plate reader (Tecan) with an excitation of 490/10 nm and an emission of 520/10 nm and

598 raw fluorescence units (RFU) were normalized to tissue weights.

599

600 *RNA isolation from pMBMECs and real time (RT) PCR*

601 Isolation of RNA from cultured pMBMECs was performed with the ReliaPrep™ RNA Cell

602 Miniprep System (Promega) following manufacturers guidelines. RNA concentrations were

603 determined by measuring absorbance using the NanoQuant Plate™ (Tecan) at an Infinite

604 M200 pro plate reader (Tecan). cDNA was synthesized using 200–1000 ng of total RNA with

605 the QuantiTect® Reverse Transcription Kit (Qiagen) and subsequently used for qPCR, which

606 was performed with the StepOnePlus™ Real-Time PCR System (Life Technologies) using SYBR

607 Green reagent (Promega). Fold enrichment was calculated using the Delta–Delta CT method

608 normalized to hypoxanthin-guanin-phosphoribosyltransferase (*Hprt*) as house-keeping

609 reference. *Tnfaip3* primer were ordered as QuantiTect Primer Assay (QT00134064, Qiagen).

610 *Icosl* primer (forward: 5'- AGGCTCCCTTGGACATCTCG -3'; reverse: 5'-

611 CAGTACAGCAAGGACGGGGA -3') were self-designed using primer-BLAST tool from the

612 National Center for Biotechnology Information (NCBI) and were synthesized by Metabion.

613

614 *Western blot*

615 Western blotting for the A20 protein was performed on primary brain endothelial cells of

616 A20$^{fl/fl}$ and A20$^{\Delta CNS-EC}$ mice. After reaching confluence, cells were lysed and western blotting

617 was performed as described before (22) using antibodies targeting A20 (A-12, mouse

618 monoclonal, Santa Cruz, 1:500) and actin (C-11, goat polyclonal, Santa Cruz, 1:1000) and

619 secondary antibodies against mouse IgG (HRP-coupled, Santa Cruz, 1:1000) and goat IgG (HRP-

620 coupled, DAKO, 1:10000), respectively.

621

622 *In vitro T cell static adhesion assay*

623

624 pMBMECs were isolated and cultured as described above for 7 days on µ-dishes (ibidi GmbH).

625 After 4 days, cells were stimulated with 20 ng/ml IL-1β for 72 h. Th1 or Th17 cells from 2D2

626 C57BL/6 mice were thawed and rested for approximately 4 h in T cell medium and

627 subsequently labelled with 1 µM CellTracker^{TM} Green (Thermo Fisher Scientific) for 30 min.

628 pMBMECs were incubated with 15 µg/ml anti-mouse ICOSL (HK5.3, rat IgG2a monoclonal,

629 BioXCell) or 15 µg/ml negative control (MJ7/18, rat IgG2a anti mouse endoglin (76)) for 30

630 min. 100,000 T cells were added to the pMBMECs and were allowed to adhere for 30 min on

631 a shaking platform. Wells were washed with PBS and fixed with 1% PFA for 10 min before

632 mounting on glass slides with DAPI. Images were acquired at an Eclipse E600 microscope

633 (Nikon) and adhering T cells were counted using ImageJ software (National Institute of

634 Health).

635

636 *In vitro T cell migration assay under physiological flow*

637 In vitro live-cell imaging of T cell diapedesis across pMBMECs was performed as described

638 before (90). In brief, pMBMECs were isolated and cultured for 7 days on µ-dishes (ibidi GmbH).

639 After 4 days, cells were stimulated with 20 ng/mL IL-1β for 72 h. 2D2 Th1 cells were

640 resuspended at 1×10^6 cells/ml in T cell medium. Prior to the experiment, pMBMECs were

641   treated with 15 μg/ml anti-mouse ICOSL (HK5.3, rat IgG2a monoclonal, BioXCell) or 15 μg/ml

642   negative control (MJ7/18, rat IgG2a anti mouse endoglin (76)) for 30 min at 37°C.

643   Accumulation of 2D2 Th1 on pMBMECs in the flow chamber was allowed for 4 min at a low

644   shear (0.1 dyn/cm^2), followed by physiological shear (1.5 dyn/cm^2) for an additional 20 min,

645   for a total recording time of 24 min. Image acquisition was performed at 10× magnification

646   with the AxioObserver inverted microscope (Carl Zeiss) with differential interference contrast

647   using the camera Evolve Delta (Teledyne Photometrics). Image frames were recorded every

648   10 s. Image analysis was performed using ImageJ software (National Institute of Health). T cell

649   post-arrest behavior was defined and expressed as described previously (91). T cell crawling

650   tracks were evaluated after manual tracking of individual T cells using the manual tracking

651   plug-in of ImageJ. Distance and speed of crawling tracks were evaluated using chemotaxis and

652   migration tool (version 2.0, Ibidi GmbH).

653

654   *Adeno-associated virus (AAV) design and applications*

655   For knockdown of ICOSL specifically in CNS-ECs AAV-BR1 (45) was used to deliver a short

656   hairpin (sh) RNA against *Icosl* carrying the sense sequence GCAGAAAGTTTCACTGGAAATCTC

657   to the target cells. The AAV-BR1-RSV-GFP-H1-shRNA_Icosl and the control AAV-BR1-RSV-GFP-

658   H1-shRNA_scrambled constructs were produced by the Viral Vector Production Unit of the

659   Universitat Autònoma Barcelona, Spain. The AAVs were delivered to us ready for use.

660   For in vitro experiments, pMBMECs grown in 48-well plates were transfected with 0.6x10^6

661   genomic particles (gp) per well four days after seeding. For in vivo experiments, constructs

662   were delivered i.v. at a concentration of 1.8x10^{11} gp in 100 μl sterile PBS. AAV-BR1-eGFP was

663   used as described elsewhere (45).

664

665 *Statistics*

666 Statistical analyses were performed with Prism v9 software (GraphPad). All values are

667 represented as mean $\pm$ standard error of the mean (SEM) unless otherwise stated. *P* values

668 were considered significant with p<0.05.

669

670 *Study approval*

671 All animal experiments were approved by the local administrations (Landesuntersuchungsamt

672 Koblenz, Germany; Ministerium für Energiewende, Landwirtschaft, Umwelt und ländliche

673 Räume, Kiel, Germany; individual approval numbers G20-1-049 and G22-1-005). Experiments

674 were performed in accordance with the guidelines from the translational animal research

675 center (TARC) Mainz, Germany. All efforts were made to minimize suffering of the mice.

676

677 *Data availability*

678 The RNA-seq data presented in this manuscript have been deposited in the Gene Expression

679 Omnibus (GEO) under accession number GSE221318. All other data is available in the

680 'Supporting data values' file.

681

682 AUTHOR CONTRIBUTIONS

683 L.J. performed experiments, analyzed data, prepared figures, and wrote the manuscript. S.S.,

684 K.M., J.L., M.A.K., J.C.A., and J.W. performed experiments and analyzed data; F.M. performed

685 bioinformatic analysis; N.R., I.P. and C.S. helped with experiments, data analysis and

686 discussion. E.S. helped with experiments and manuscript writing. M.K. and T.B. provided

687 reagents and guided preparation of samples for RNA seq. K.K. helped with histology and

688 confocal imaging. M.H.H.S., D.S. and G.v.L. provided mouse strains. J.K. provided the AAV-BR1

689   plasmid. B.E. and M.S. were associated with conceptualization and supervision of the project,

690   funding acquisition, and finalization of the manuscript. A.W. supervised the project, acquired

691   funding and wrote the manuscript together with L.J.

692

705

706   REFERENCES

707   1.   Multiple-Sclerosis-International-Federation. The Atlas of MS. 2022.
708   https://www.msif.org/news/2021/04/27/the-atlas-of-ms-part-2-goes-live/
709   2.   Baecher-Allan C, et al. Multiple Sclerosis: Mechanisms and Immunotherapy. *Neuron*.
710   Feb 21 2018;97(4):742-768. doi:10.1016/j.neuron.2018.01.021
711   3.   Lassmann H. Multiple Sclerosis Pathology. *Cold Spring Harb Perspect Med*. Mar 1
712   2018;8(3)doi:10.1101/cshperspect.a028936
713   4.   Waisman A, Johann L. Antigen-presenting cell diversity for T cell reactivation in
714   central nervous system autoimmunity. *J Mol Med (Berl)*. Dec 2018;96(12):1279-1292.
715   doi:10.1007/s00109-018-1709-7
716   5.   Engelhardt B, et al. Vascular, glial, and lymphatic immune gateways of the central
717   nervous system. *Acta Neuropathol*. Sep 2016;132(3):317-38. doi:10.1007/s00401-016-1606-
718   5
719   6.   Engelhardt B, Ransohoff RM. Capture, crawl, cross: the T cell code to breach the
720   blood-brain barriers. *Trends Immunol*. Dec 2012;33(12):579-89. doi:10.1016/j.it.2012.07.004
721   7.   Engelhardt B, et al. The movers and shapers in immune privilege of the CNS. *Nat
722   Immunol*. Feb 2017;18(2):123-131. doi:10.1038/ni.3666
723   8.   Lou J, et al. Direct cell/cell contact with stimulated T lymphocytes induces the
724   expression of cell adhesion molecules and cytokines by human brain microvascular
725   endothelial cells. *Eur J Immunol*. Dec 1996;26(12):3107-13. doi:10.1002/eji.1830261242
726   9.   Carrithers MD, et al. Differential adhesion molecule requirements for immune
727   surveillance and inflammatory recruitment. *Brain*. Jun 2000;123 (Pt 6):1092-101.
728   doi:10.1093/brain/123.6.1092
729   10.   Munji RN, et al. Profiling the mouse brain endothelial transcriptome in health and
730   disease models reveals a core blood-brain barrier dysfunction module. *Nat Neurosci*. Nov
731   2019;22(11):1892-1902. doi:10.1038/s41593-019-0497-x
732   11.   Profaci CP, et al. The blood-brain barrier in health and disease: Important
733   unanswered questions. *J Exp Med*. Apr 6 2020;217(4)doi:10.1084/jem.20190062
734   12.   Jeong HW, et al. Single-cell transcriptomics reveals functionally specialized vascular
735   endothelium in brain. *Elife*. Oct 5 2022;11doi:10.7554/eLife.57520
736   13.   Hauptmann J, et al. Interleukin-1 promotes autoimmune neuroinflammation by
737   suppressing endothelial heme oxygenase-1 at the blood-brain barrier. *Acta Neuropathol*. Oct
738   2020;140(4):549-567. doi:10.1007/s00401-020-02187-x
739   14.   Thornton P, et al. Interleukin-1 drives cerebrovascular inflammation via MAP kinase-
740   independent pathways. *Curr Neurovasc Res*. Nov 2010;7(4):330-40.
741   doi:10.2174/156720210793180800
742   15.   Ledebur HC, Parks TP. Transcriptional regulation of the intercellular adhesion
743   molecule-1 gene by inflammatory cytokines in human endothelial cells. Essential roles of a
744   variant NF-kappa B site and p65 homodimers. *J Biol Chem*. Jan 13 1995;270(2):933-43.
745   doi:10.1074/jbc.270.2.933
746   16.   Wertheimer SJ, et al. Intercellular adhesion molecule-1 gene expression in human
747   endothelial cells. Differential regulation by tumor necrosis factor-alpha and phorbol
748   myristate acetate. *J Biol Chem*. Jun 15 1992;267(17):12030-5.
749   17.   Neish AS, et al. Functional analysis of the human vascular cell adhesion molecule 1
750   promoter. *J Exp Med*. Dec 1 1992;176(6):1583-93. doi:10.1084/jem.176.6.1583

751 18. Shu HB, et al. Differential regulation of vascular cell adhesion molecule 1 gene
752 expression by specific NF-kappa B subunits in endothelial and epithelial cells. *Mol Cell Biol*.
753 Oct 1993;13(10):6283-9. doi:10.1128/mcb.13.10.6283-6289.1993
754 19. Tripathi AK, et al. Plasmodium falciparum-infected erythrocytes induce NF-kappaB
755 regulated inflammatory pathways in human cerebral endothelium. *Blood*. Nov 5
756 2009;114(19):4243-52. doi:10.1182/blood-2009-06-226415
757 20. Jacob A, et al. C5a/CD88 signaling alters blood-brain barrier integrity in lupus through
758 nuclear factor-kappaB. *J Neurochem*. Dec 2011;119(5):1041-51. doi:10.1111/j.1471-
759 4159.2011.07490.x
760 21. Kielland A, et al. NF-kappaB activity in perinatal brain during infectious and hypoxic-
761 ischemic insults revealed by a reporter mouse. *Brain Pathol*. Jul 2012;22(4):499-510.
762 doi:10.1111/j.1750-3639.2011.00548.x
763 22. Ridder DA, et al. Brain endothelial TAK1 and NEMO safeguard the neurovascular unit.
764 *J Exp Med*. Sep 21 2015;212(10):1529-49. doi:10.1084/jem.20150165
765 23. Opipari AW, Jr., et al. The A20 zinc finger protein protects cells from tumor necrosis
766 factor cytotoxicity. *J Biol Chem*. Jun 25 1992;267(18):12424-7.
767 24. Cooper JT, et al. A20 blocks endothelial cell activation through a NF-kappaB-
768 dependent mechanism. *J Biol Chem*. Jul 26 1996;271(30):18068-73.
769 doi:10.1074/jbc.271.30.18068
770 25. Tewari M, et al. Lymphoid expression and regulation of A20, an inhibitor of
771 programmed cell death. *J Immunol*. Feb 15 1995;154(4):1699-706.
772 26. International Multiple Sclerosis Genetics C, et al. Analysis of immune-related loci
773 identifies 48 new susceptibility variants for multiple sclerosis. *Nat Genet*. Nov
774 2013;45(11):1353-60. doi:10.1038/ng.2770
775 27. Guedes RP, et al. A20 deficiency causes spontaneous neuroinflammation in mice. *J
776 Neuroinflammation*. Jul 16 2014;11:122. doi:10.1186/1742-2094-11-122
777 28. Wang X, et al. Astrocytic A20 ameliorates experimental autoimmune
778 encephalomyelitis by inhibiting NF-kappaB- and STAT1-dependent chemokine production in
779 astrocytes. *Acta Neuropathol*. Nov 2013;126(5):711-724. doi:10.1007/s00401-013-1183-9
780 29. Voet S, et al. A20 critically controls microglia activation and inhibits inflammasome-
781 dependent neuroinflammation. *Nat Commun*. May 23 2018;9(1):2036. doi:10.1038/s41467-
782 018-04376-5
783 30. Mohebiany AN, et al. Microglial A20 Protects the Brain from CD8 T-Cell-Mediated
784 Immunopathology. *Cell Rep*. Feb 4 2020;30(5):1585-1597 e6.
785 doi:10.1016/j.celrep.2019.12.097
786 31. Zhang Y, et al. An RNA-sequencing transcriptome and splicing database of glia,
787 neurons, and vascular cells of the cerebral cortex. *J Neurosci*. Sep 3 2014;34(36):11929-47.
788 doi:10.1523/JNEUROSCI.1860-14.2014
789 32. Ridder DA, et al. TAK1 in brain endothelial cells mediates fever and lethargy. *J Exp
790 Med*. Dec 19 2011;208(13):2615-23. doi:10.1084/jem.20110398
791 33. Wang Y, et al. Ephrin-B2 controls VEGF-induced angiogenesis and lymphangiogenesis.
792 *Nature*. May 27 2010;465(7297):483-6. doi:10.1038/nature09002
793 34. Koutrolos M, et al. Treg cells mediate recovery from EAE by controlling effector T cell
794 proliferation and motility in the CNS. *Acta Neuropathol Commun*. Dec 5 2014;2:163.
795 doi:10.1186/s40478-014-0163-1
796 35. Brown WR. A review of string vessels or collapsed, empty basement membrane
797 tubes. *J Alzheimers Dis*. 2010;21(3):725-39. doi:10.3233/JAD-2010-100219

798   36.   Abadier M, et al. Cell surface levels of endothelial ICAM-1 influence the transcellular
799   or paracellular T-cell diapedesis across the blood-brain barrier. *Eur J Immunol*. Apr
800   2015;45(4):1043-58. doi:10.1002/eji.201445125
801   37.   Polman CH, et al. A randomized, placebo-controlled trial of natalizumab for relapsing
802   multiple sclerosis. *N Engl J Med*. Mar 2 2006;354(9):899-910. doi:10.1056/NEJMoa044397
803   38.   Rudick RA, et al. Natalizumab plus interferon beta-1a for relapsing multiple sclerosis.
804   *N Engl J Med*. Mar 2 2006;354(9):911-23. doi:10.1056/NEJMoa044396
805   39.   Havrdova E, et al. Effect of natalizumab on clinical and radiological disease activity in
806   multiple sclerosis: a retrospective analysis of the Natalizumab Safety and Efficacy in
807   Relapsing-Remitting Multiple Sclerosis (AFFIRM) study. *Lancet Neurol*. Mar 2009;8(3):254-60.
808   doi:10.1016/S1474-4422(09)70021-3
809   40.   Bloomgren G, et al. Risk of natalizumab-associated progressive multifocal
810   leukoencephalopathy. *N Engl J Med*. May 17 2012;366(20):1870-80.
811   doi:10.1056/NEJMoa1107829
812   41.   Caravagna C, et al. Diversity of innate immune cell subsets across spatial and
813   temporal scales in an EAE mouse model. *Sci Rep*. Mar 23 2018;8(1):5146.
814   doi:10.1038/s41598-018-22872-y
815   42.   Hovelmeyer N, et al. A20 deficiency in B cells enhances B-cell proliferation and results
816   in the development of autoantibodies. *Eur J Immunol*. Mar 2011;41(3):595-601.
817   doi:10.1002/eji.201041313
818   43.   Khayyamian S, et al. ICOS-ligand, expressed on human endothelial cells, costimulates
819   Th1 and Th2 cytokine secretion by memory CD4+ T cells. *Proc Natl Acad Sci U S A*. Apr 30
820   2002;99(9):6198-203. doi:10.1073/pnas.092576699
821   44.   Wheway J, et al. The brain microvascular endothelium supports T cell proliferation
822   and has potential for alloantigen presentation. *PLoS One*. 2013;8(1):e52586.
823   doi:10.1371/journal.pone.0052586
824   45.   Korbelin J, et al. A brain microvasculature endothelial cell-specific viral vector with
825   the potential to treat neurovascular and neurological diseases. *EMBO Mol Med*. Jun
826   2016;8(6):609-25. doi:10.15252/emmm.201506078
827   46.   Ansari AM, et al. Cellular GFP Toxicity and Immunogenicity: Potential Confounders in
828   in Vivo Cell Tracking Experiments. *Stem Cell Rev Rep*. Oct 2016;12(5):553-559.
829   doi:10.1007/s12015-016-9670-8
830   47.   Barclay AN. Membrane proteins with immunoglobulin-like domains--a master
831   superfamily of interaction molecules. *Semin Immunol*. Aug 2003;15(4):215-23.
832   doi:10.1016/s1044-5323(03)00047-2
833   48.   Lecuyer MA, et al. Dual role of ALCAM in neuroinflammation and blood-brain barrier
834   homeostasis. *Proc Natl Acad Sci U S A*. Jan 24 2017;114(4):E524-E533.
835   doi:10.1073/pnas.1614336114
836   49.   Michel L, et al. Activated leukocyte cell adhesion molecule regulates B lymphocyte
837   migration across central nervous system barriers. *Sci Transl Med*. Nov 13
838   2019;11(518)doi:10.1126/scitranslmed.aaw0475
839   50.   Larochelle C, et al. Melanoma cell adhesion molecule identifies encephalitogenic T
840   lymphocytes and promotes their recruitment to the central nervous system. *Brain*. Oct
841   2012;135(Pt 10):2906-24. doi:10.1093/brain/aws212
842   51.   Larochelle C, et al. Melanoma cell adhesion molecule-positive CD8 T lymphocytes
843   mediate central nervous system inflammation. *Ann Neurol*. Jul 2015;78(1):39-53.
844   doi:10.1002/ana.24415

845   52.   Charabati M, et al. DICAM promotes TH17 lymphocyte trafficking across the blood-
846   brain barrier during autoimmune neuroinflammation. *Sci Transl Med*. Jan 5
847   2022;14(626):eabj0473. doi:10.1126/scitranslmed.abj0473
848   53.   Du F, et al. Inflammatory Th17 Cells Express Integrin alphavbeta3 for Pathogenic
849   Function. *Cell Rep*. Aug 2 2016;16(5):1339-1351. doi:10.1016/j.celrep.2016.06.065
850   54.   Koh KH, et al. Nonimmune cell-derived ICOS ligand functions as a renoprotective
851   alphavbeta3 integrin-selective antagonist. *J Clin Invest*. Apr 1 2019;129(4):1713-1726.
852   doi:10.1172/JCI123386
853   55.   Dopp JM, et al. Expression of ICAM-1, VCAM-1, L-selectin, and leukosialin in the
854   mouse central nervous system during the induction and remission stages of experimental
855   allergic encephalomyelitis. *J Neuroimmunol*. Oct 1994;54(1-2):129-44. doi:10.1016/0165-
856   5728(94)90239-9
857   56.   Lee SJ, Benveniste EN. Adhesion molecule expression and regulation on cells of the
858   central nervous system. *J Neuroimmunol*. Aug 3 1999;98(2):77-88. doi:10.1016/s0165-
859   5728(99)00084-3
860   57.   Alvarez JI, et al. Disruption of central nervous system barriers in multiple sclerosis.
861   *Biochim Biophys Acta*. Feb 2011;1812(2):252-64. doi:10.1016/j.bbadis.2010.06.017
862   58.   Larochelle C, et al. How do immune cells overcome the blood-brain barrier in
863   multiple sclerosis? *FEBS Lett*. Dec 1 2011;585(23):3770-80.
864   doi:10.1016/j.febslet.2011.04.066
865   59.   Merrill JE, Murphy SP. Inflammatory events at the blood brain barrier: regulation of
866   adhesion molecules, cytokines, and chemokines by reactive nitrogen and oxygen species.
867   *Brain Behav Immun*. Dec 1997;11(4):245-63. doi:10.1006/brbi.1997.0496
868   60.   O'Carroll SJ, et al. Pro-inflammatory TNFalpha and IL-1beta differentially regulate the
869   inflammatory phenotype of brain microvascular endothelial cells. *J Neuroinflammation*. Jul 8
870   2015;12:131. doi:10.1186/s12974-015-0346-0
871   61.   Levesque SA, et al. Myeloid cell transmigration across the CNS vasculature triggers IL-
872   1beta-driven neuroinflammation during autoimmune encephalomyelitis in mice. *J Exp Med*.
873   May 30 2016;213(6):929-49. doi:10.1084/jem.20151437
874   62.   Saitou M, et al. Occludin-deficient embryonic stem cells can differentiate into
875   polarized epithelial cells bearing tight junctions. *J Cell Biol*. Apr 20 1998;141(2):397-408.
876   doi:10.1083/jcb.141.2.397
877   63.   Saitou M, et al. Complex phenotype of mice lacking occludin, a component of tight
878   junction strands. *Mol Biol Cell*. Dec 2000;11(12):4131-42. doi:10.1091/mbc.11.12.4131
879   64.   Yu AS, et al. Knockdown of occludin expression leads to diverse phenotypic
880   alterations in epithelial cells. *Am J Physiol Cell Physiol*. Jun 2005;288(6):C1231-41.
881   doi:10.1152/ajpcell.00581.2004
882   65.   Schulzke JD, et al. Epithelial transport and barrier function in occludin-deficient mice.
883   *Biochim Biophys Acta*. May 15 2005;1669(1):34-42. doi:10.1016/j.bbamem.2005.01.008
884   66.   Daems CSMVVvLGDHRC-VZCP. A20/TNFAIP3 heterozygosity predisposes to
885   behavioral symptoms in a mouse model for neuropsychiatric lupus. *Brain, Behavior, &*
886   *Immunity - Health*. 2020;
887   67.   Gelderblom M, et al. Neutralization of the IL-17 axis diminishes neutrophil invasion
888   and protects from ischemic stroke. *Blood*. Nov 1 2012;120(18):3793-802. doi:10.1182/blood-
889   2012-02-412726
890   68.   Liesz A, et al. Inhibition of lymphocyte trafficking shields the brain against deleterious
891   neuroinflammation after stroke. *Brain*. Mar 2011;134(Pt 3):704-20.
892   doi:10.1093/brain/awr008

893   69.   Neumann J, et al. Very-late-antigen-4 (VLA-4)-mediated brain invasion by neutrophils
894   leads to interactions with microglia, increased ischemic injury and impaired behavior in
895   experimental stroke. *Acta Neuropathol*. Feb 2015;129(2):259-77. doi:10.1007/s00401-014-
896   1355-2
897   70.   Lyck R, et al. ALCAM (CD166) is involved in extravasation of monocytes rather than T
898   cells across the blood-brain barrier. *J Cereb Blood Flow Metab*. Aug 2017;37(8):2894-2909.
899   doi:10.1177/0271678X16678639
900   71.   Schneider-Hohendorf T, et al. VLA-4 blockade promotes differential routes into
901   human CNS involving PSGL-1 rolling of T cells and MCAM-adhesion of TH17 cells. *J Exp Med*.
902   Aug 25 2014;211(9):1833-46. doi:10.1084/jem.20140540
903   72.   Charabati M, et al. MCAM+ brain endothelial cells contribute to neuroinflammation
904   by recruiting pathogenic CD4+ T lymphocytes. *Brain*. Apr 19 2023;146(4):1483-1495.
905   doi:10.1093/brain/awac389
906   73.   Roussel L, et al. Loss of human ICOSL results in combined immunodeficiency. *J Exp
907   Med*. Dec 3 2018;215(12):3151-3164. doi:10.1084/jem.20180668
908   74.   Schlager C, et al. Effector T-cell trafficking between the leptomeninges and the
909   cerebrospinal fluid. *Nature*. Feb 18 2016;530(7590):349-53. doi:10.1038/nature16939
910   75.   Bartholomaus I, et al. Effector T cell interactions with meningeal vascular structures
911   in nascent autoimmune CNS lesions. *Nature*. Nov 5 2009;462(7269):94-8.
912   doi:10.1038/nature08478
913   76.   Engelhardt B, et al. The development of experimental autoimmune
914   encephalomyelitis in the mouse requires alpha4-integrin but not alpha4beta7-integrin. *J Clin
915   Invest*. Dec 15 1998;102(12):2096-105. doi:10.1172/JCI4271
916   77.   Dong C, et al. ICOS co-stimulatory receptor is essential for T-cell activation and
917   function. *Nature*. Jan 4 2001;409(6816):97-101. doi:10.1038/35051100
918   78.   Mak TW, et al. Costimulation through the inducible costimulator ligand is essential
919   for both T helper and B cell functions in T cell-dependent B cell responses. *Nat Immunol*. Aug
920   2003;4(8):765-72. doi:10.1038/ni947
921   79.   Coyle AJ, et al. The CD28-related molecule ICOS is required for effective T cell-
922   dependent immune responses. *Immunity*. Jul 2000;13(1):95-105. doi:10.1016/s1074-
923   7613(00)00011-x
924   80.   Rottman JB, et al. The costimulatory molecule ICOS plays an important role in the
925   immunopathogenesis of EAE. *Nat Immunol*. Jul 2001;2(7):605-11. doi:10.1038/89750
926   81.   Galicia G, et al. ICOS deficiency results in exacerbated IL-17 mediated experimental
927   autoimmune encephalomyelitis. *J Clin Immunol*. Jul 2009;29(4):426-33. doi:10.1007/s10875-
928   009-9287-7
929   82.   Vereecke L, et al. Enterocyte-specific A20 deficiency sensitizes to tumor necrosis
930   factor-induced toxicity and experimental colitis. *J Exp Med*. Jul 5 2010;207(7):1513-23.
931   doi:10.1084/jem.20092474
932   83.   Srinivas S, et al. Cre reporter strains produced by targeted insertion of EYFP and ECFP
933   into the ROSA26 locus. *BMC Dev Biol*. 2001;1:4. doi:10.1186/1471-213x-1-4
934   84.   Chen H, et al. Hydroxycarboxylic acid receptor 2 mediates dimethyl fumarate's
935   protective effect in EAE. *J Clin Invest*. May 2014;124(5):2188-92. doi:10.1172/JCI72151
936   85.   Wenzel J, et al. Endogenous THBD (Thrombomodulin) Mediates Angiogenesis in the
937   Ischemic Brain-Brief Report. *Arterioscler Thromb Vasc Biol*. Dec 2020;40(12):2837-2844.
938   doi:10.1161/ATVBAHA.120.315061

939   86.   Lubjuhn J, et al. Functional testing in a mouse stroke model induced by occlusion of
940   the distal middle cerebral artery. *J Neurosci Methods*. Oct 30 2009;184(1):95-103.
941   doi:10.1016/j.jneumeth.2009.07.029
942   87.   Coisne C, et al. Mouse syngenic in vitro blood-brain barrier model: a new tool to
943   examine inflammatory events in cerebral endothelium. *Lab Invest*. Jun 2005;85(6):734-46.
944   doi:10.1038/labinvest.3700281
945   88.   Ludt A, et al. Interactive and Reproducible Workflows for Exploring and Modeling
946   RNA-seq Data with pcaExplorer, Ideal, and GeneTonic. *Curr Protoc*. Apr 2022;2(4):e411.
947   doi:10.1002/cpz1.411
948   89.   Marini F, et al. GeneTonic: an R/Bioconductor package for streamlining the
949   interpretation of RNA-seq data. *BMC Bioinformatics*. Dec 23 2021;22(1):610.
950   doi:10.1186/s12859-021-04461-5
951   90.   Coisne C, et al. Live cell imaging techniques to study T cell trafficking across the
952   blood-brain barrier in vitro and in vivo. *Fluids Barriers CNS*. Jan 21 2013;10(1):7.
953   doi:10.1186/2045-8118-10-7
954   91.   Marchetti L, et al. ACKR1 favors transcellular over paracellular T-cell diapedesis
955   across the blood-brain barrier in neuroinflammation in vitro. *Eur J Immunol*. Jan
956   2022;52(1):161-177. doi:10.1002/eji.202149238
957
958

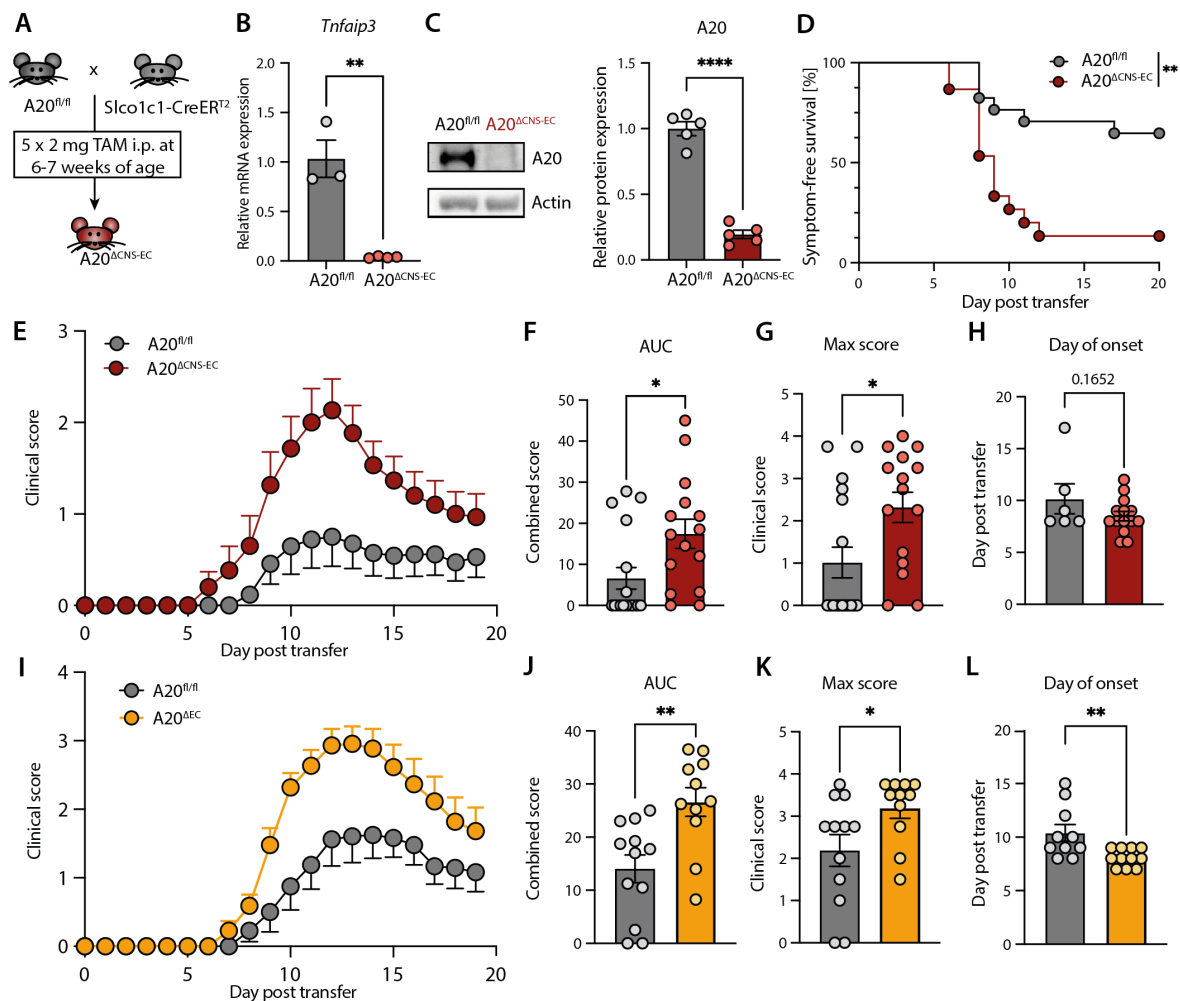*Figure 1: CNS EC-A20 plays a protective role in CNS autoimmunity*

(A) Breeding strategy for generation of A20^ΔCNS-EC mice. Conditional deletion of *Tnfaip3* in A20^ΔCNS-EC mice is achieved through tamoxifen (TAM) injections. (B) Validation of *Tnfaip3* deletion in pMBMECs from A20^ΔCNS-EC mice by RT-PCR. *Tnfaip3* mRNA levels are presented relative to control (n = 3-4 mice per group). (C) Western blot analysis of A20 protein in cultured primary brain endothelial cells from A20^ΔCNS-EC and littermate control mice. Protein expression of A20 is normalized to actin levels and presented relative to the expression in controls (n = 5 mice per group). (D-H) Adoptive transfer (AT)-EAE disease in A20^ΔCNS-EC mice and A20^fl/fl littermate. Clinical signs of EAE were monitored daily. Data is pooled from two independent experiments with n = 15-17 mice per group. (D) Probability of symptom-free survival is shown as Kaplan Meier curve. (E) Clinical signs of EAE are shown as mean clinical disease scores +/- SEM. (F) Area under the curve (AUC), (G) maximum clinical scores and (H) day of onset analyses of clinical course shown in (E). Every circle represents a single mouse. (I-L) AT-EAE disease was induced in A20^ΔEC lacking A20 in all endothelial cells driven by the Cdh5-CreER^T2 and A20^fl/fl littermate controls as described before. Clinical signs of EAE were monitored daily. Data is pooled from two independent experiments with n = 11-12 mice per group. (I) Clinical signs of EAE are shown as mean clinical disease scores +/- SEM. (J) AUC, (K) maximum clinical scores and (L) day of onset analyses of clinical course shown in (I). Every circle represents a single mouse. Statistical significance was determined by two-tailed unpaired Student's t-test (B, C, F-H, J-L) or Log-rank (Mantel-Cox) test (D). * $p<0.05$, ** $p<0.01$, **** $p<0.0001$.
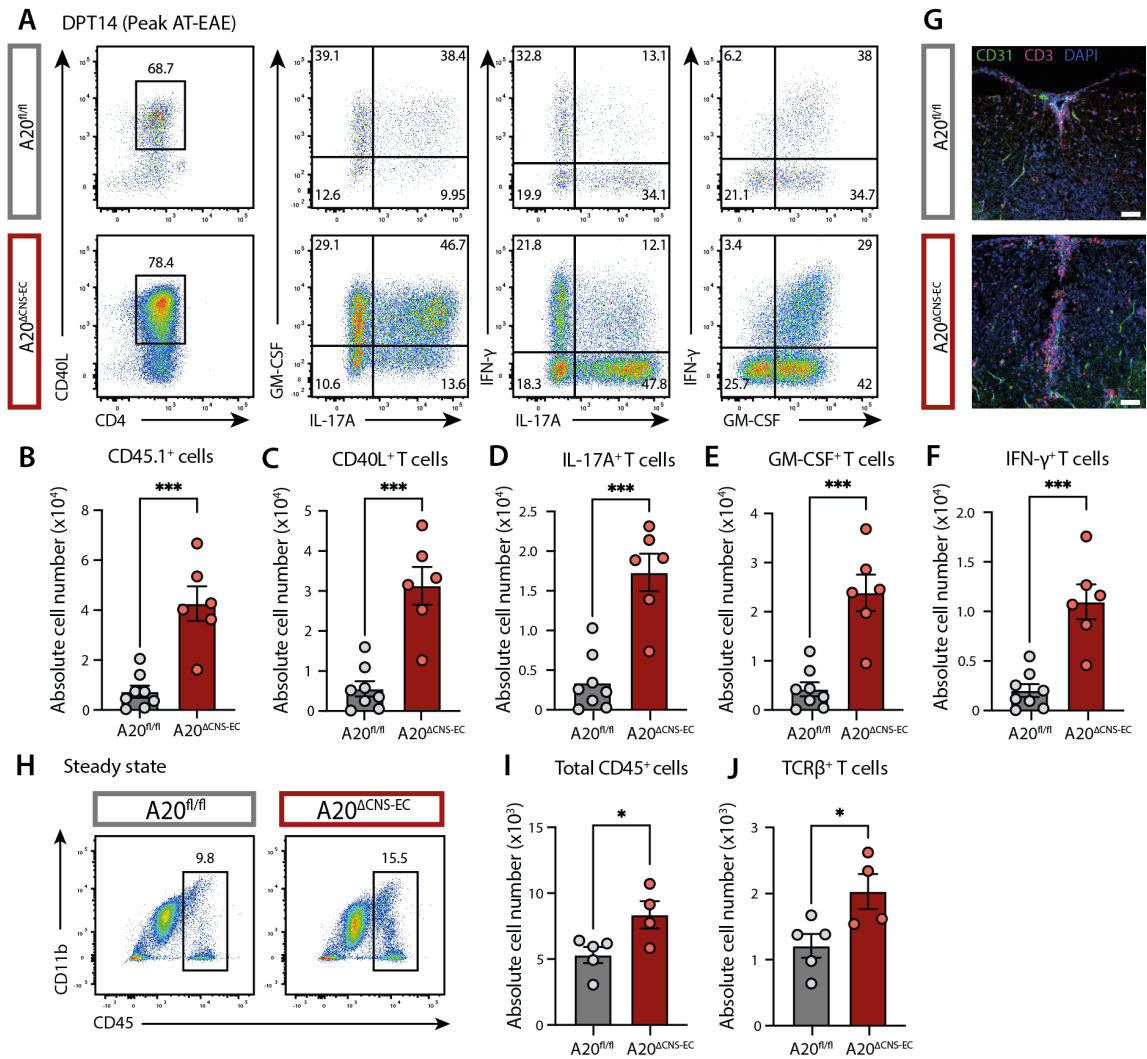
Figure 2: Loss of CNS EC-A20 drives T cell infiltration during EAE and in the steady state

(A-E) AT-EAE disease was induced in A20$^{\Delta CNS-EC}$ mice and A20$^{fl/fl}$ littermate controls. At the peak of the disease (day post transfer (DPT) 14) SC-infiltrating CD45.1$^+$ transferred T cells were isolated and analyzed by flow cytometry after a MOG recall assay *ex vivo*. (A) Representative gating strategy for CD40L$^+$ CD4$^+$ T cells and amongst them frequencies of GM-CSF, IL-17A, IFN-γ and double-producing cells; pre-gated as single, live, CD45.1$^+$ transferred T cells. (B-F) Quantification of immune cell populations. Data is representative for 2 independent experiments with n = 6-8 mice per group. (B) Absolute cell numbers of CD45.1$^+$ transferred T cells, (C) CD40L$^+$ among transferred T cells, (D) IL-17A$^+$, (E) GM-CSF$^+$ and (F) IFN-γ$^+$ cells amongst CD40L$^+$ cells. (G) Representative immunostainings of CD3$^+$ T cells (magenta), CD31$^+$ endothelial cells (green) and nuclear staining (DAPI, blue) in the SC at the peak of AT-EAE (DPT14) of A20$^{\Delta CNS-EC}$ and A20$^{fl/fl}$ mice (scale bar = 50 μm). (H-J) Flow cytometric analysis of CNS-infiltrating cells in the steady state of A20$^{\Delta CNS-EC}$ and A20$^{fl/fl}$ mice one week after TAM treatment. Cells were isolated from pooled SC and brain tissue. (H) Representative gating strategy for CD45$^+$ total immune cells; pre-gated as single, live cells. (I-J) Quantification of immune cell populations. Data is representative for 3 independent experiments with n = 4-5 mic per group. (I) Absolute cell numbers of CD45$^+$ total infiltrates and amongst them (J) number of TCRβ$^+$ T cells. Statistical significance was determined by two-tailed unpaired Student's t-test. * p<0.05, *** p<0.001.
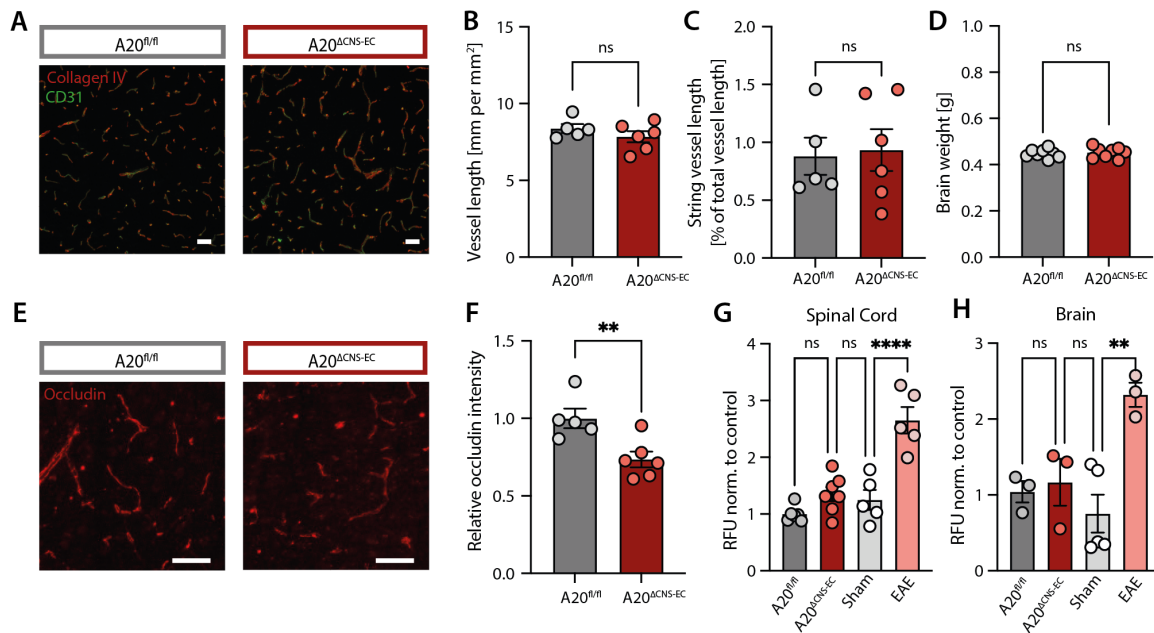
39

1003
1004 *Figure 3: A20-deficiency in CNS-ECs does not impair BBB integrity*
1005 (A-C) Brain sections from A20$^{\Delta CNS-EC}$ and A20$^{fl/fl}$ mice were stained for collagen IV (red) and
1006 CD31 (green) to determine vessel length and string vessel length. String vessels were identified
1007 as capillaries that have lost CD31-positive endothelial cells and only consist of the basement
1008 membrane protein collagen IV. Representative microscopic images are shown in (A). Scale bar
1009 = 50 μm. (B) Vessel length in mm per mm^2 and (C) string vessel length [%] normalized to A20$^{fl/fl}$
1010 littermate controls were quantified (n = 5-6 mice per group). (D) Brain weight of A20$^{\Delta CNS-EC}$ and
1011 A20$^{fl/fl}$ mice (n = 8 mice per group) shown as representative of 2 individual cohorts. (E-F) Brain
1012 sections from A20$^{\Delta CNS-EC}$ and A20$^{fl/fl}$ mice were stained for occludin (red). Representative
1013 microscopic images are shown in (E). Scale bar = 50 μm. (F) Occludin intensity was quantified
1014 and is presented relative to A20$^{fl/fl}$ littermate control mice (n = 5-6 mice per group) as
1015 representative of 2 individual cohorts. (G-H) A20$^{\Delta CNS-EC}$ and A20$^{fl/fl}$ mice were injected with 2
1016 mM 3-5 kDa FITC-dextran in PBS i.p. After 15 minutes, SC and brain were isolated and
1017 homogenized in PBS. Fluorescence was measured in the supernatant and raw fluorescence
1018 units (RFU) were normalized to tissue weight. PBS injected mice were used as Sham controls;
1019 mice at the peak of an active EAE (scores between 1.5 – 3.5) were used as positive controls.
1020 Normalized RFUs are shown for SC (G) and brain (H) relative to A20$^{fl/fl}$ controls (SC: n = 5-7;
1021 brain: n = 3-5 mice per group). Statistical significance was determined by two-tailed unpaired
1022 Student's t-test (B-D, F) or ordinary one-way ANOVA with Tukey's multiple comparisons test
1023 (G, H). Ns = not significant, ** $p<0.01$, **** $p<0.0001$.
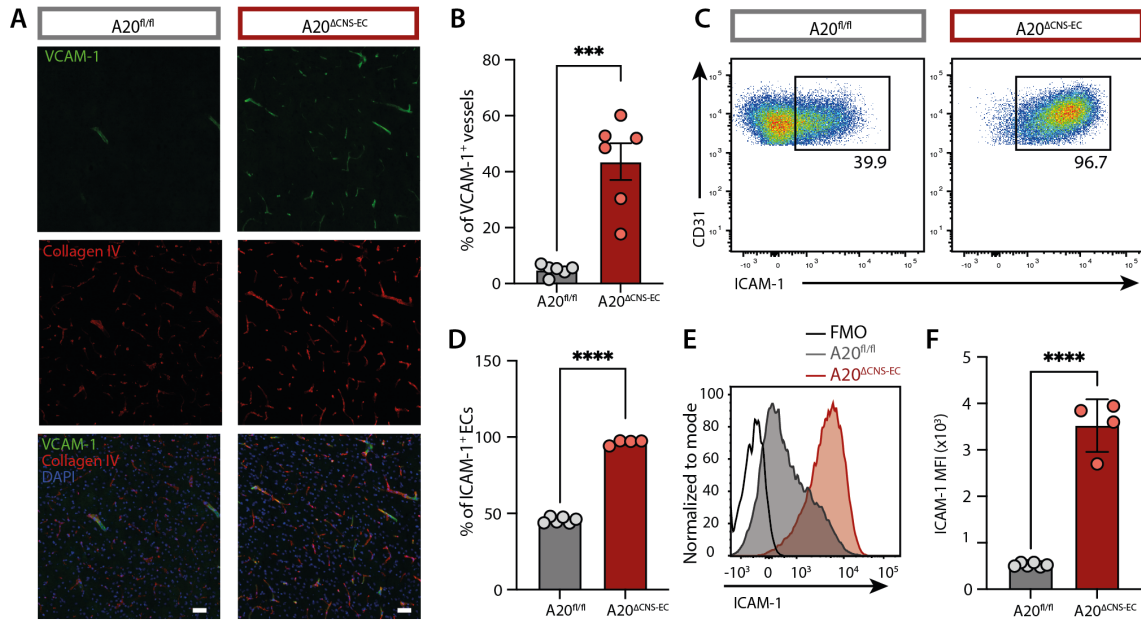1024
1025

40

Figure 4: *A20-deficiency in CNS-ECs drives adhesion molecule expression*

(A-B) Brain sections were stained for VCAM-1 (green) and collagen IV (red) together with a nuclear staining (DAPI, blue). Representative microscopic images are shown in (A). Scale bar = 50 μm. (B) Frequency of VCAM-1$^+$ vessels quantified as percentage of all collagen IV positive vessels (n = 6 mice per group). (C-F) Flow cytometric analysis of ICAM-1 on CNS-ECs isolated from pooled brain and spinal cord tissue from A20$^{\Delta CNS-EC}$ and A20$^{fl/fl}$ littermate control mice. Data is representative from 3 individual experiments with n = 4-6 mice per group. (C) Representative gating strategy for ICAM-1$^+$ CNS-ECs; gate was set based on fluorescence minus one (FMO) control. CNS-ECs were pre-gated as single, live, CD45$^-$ CD11b$^-$ Ly6C$^+$ CD31$^+$ cells. (D) Frequency of ICAM-1$^+$ ECs quantified as percentage of all CNS-ECs. (E) Histogram of ICAM-1 fluorescence on ECs in A20$^{\Delta CNS-EC}$, A20$^{fl/fl}$ mice and FMO control. (F) Mean fluorescence intensity (MFI) presented as geometric mean of ICAM-1 on CNS-ECs. Statistical significance was determined by two-tailed unpaired Student's t-test (B, D, F). *** $p<0.001$, **** $p<0.0001$.
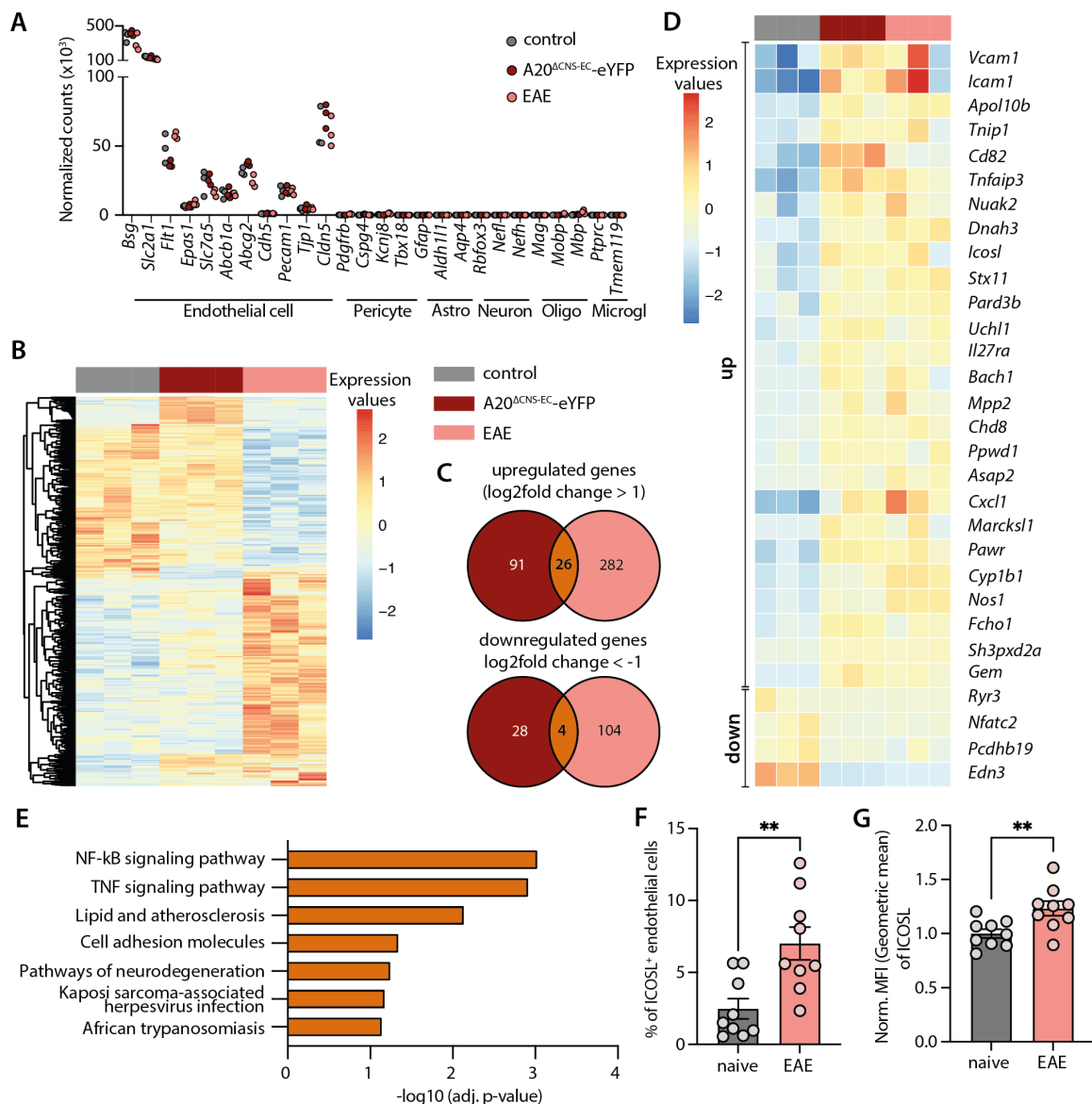
Figure 5: RNA sequencing identifies A20-regulated ICOSL as potential adhesion molecule

(A-E) RNA sequencing of sorted CNS-ECs from SC of naïve A20$^{\Delta CNS-EC}$-eYFP (red), A20$^{fl/fl}$ littermate control mice (referred to as control, grey), and A20$^{fl/fl}$ mice at day 10 after EAE immunization with MOG$_{35-55}$/CFA and PTx (referred to as EAE, pink) (n = 3 mice per group). (A) Purity of EC sorting was assessed by plotting normalized counts for marker genes of ECs, pericytes, astrocytes (astro), neurons, oligodendrocytes (oligo) and microglia (microgl). (B) Heatmap showing color-coded standardized z-scores for the expression values of genes differentially regulated in A20$^{\Delta CNS-EC}$ or EAE CNS-ECs compared to control. Each column represents an individual mouse. (C) Venn diagrams showing the number of commonly upregulated (log2fold change > 1) and commonly downregulated (log2fold change < -1) genes in A20$^{\Delta CNS-EC}$-eYFP and EAE mice compared to control as overlap of the circles. (D) Heatmap showing color-coded standardized z-scores for the expression values of the 30 commonly DE genes. Each column represents an individual mouse. (E) KEGG pathway analysis of the 30 commonly differentially expressed genes shown in (D). (F-G) ECs were isolated from the CNS of wildtype mice at day 10 post immunization with MOG$_{35-55}$/CFA and PTx or from naïve mice and stained for flow cytometric analysis of ICOSL. Data is pooled from 3 individual experiments with n = 9 mice per group. (F) Percentage and (G) normalized geometric MFI of ICOSL amongst

1060 all ECs were quantified. Statistical significance was determined by two-tailed unpaired
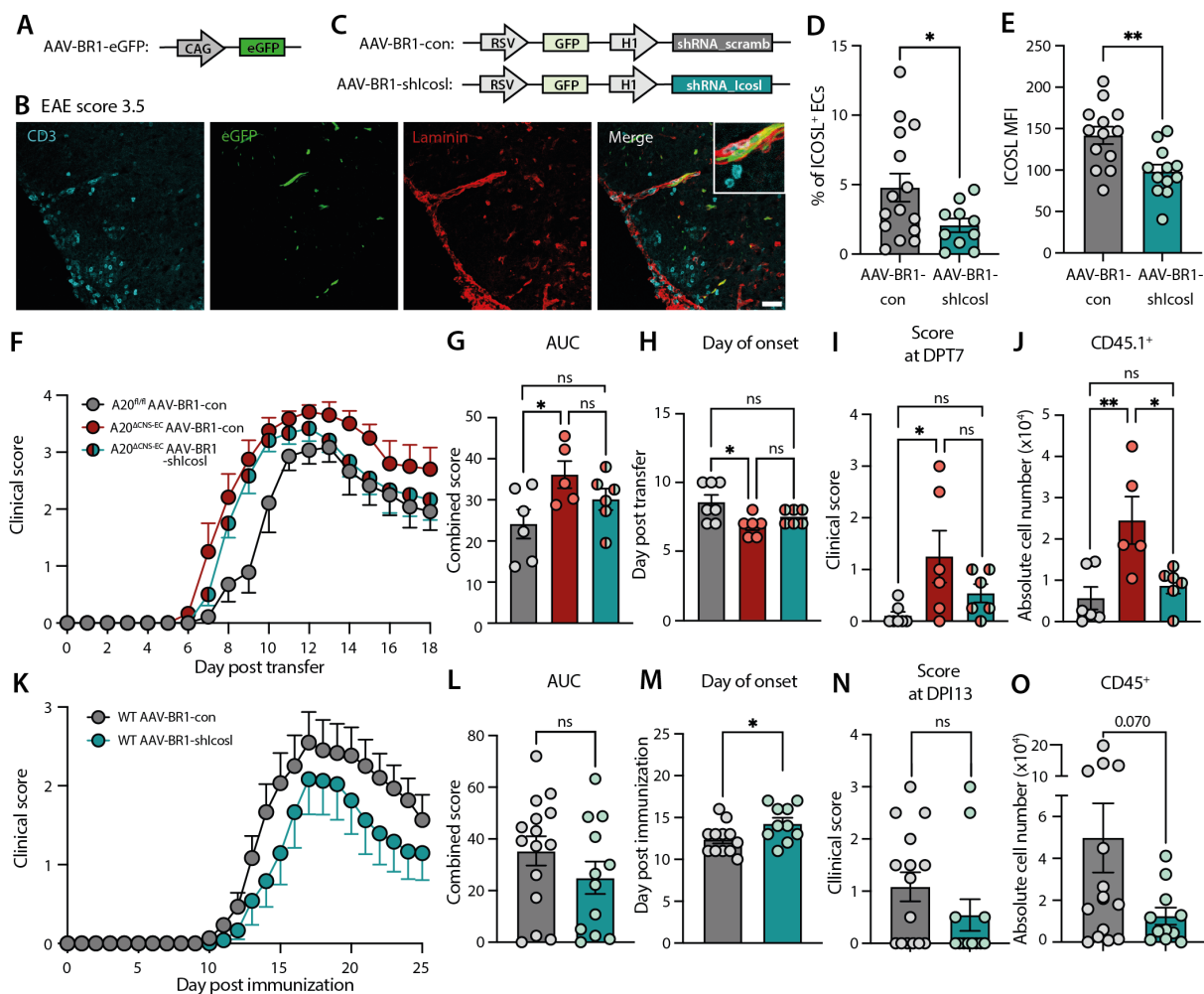1061 Student's t-test. ** p<0.01.

Figure 6: Knockdown of ICOSL on CNS microvascular ECs mildly ameliorates EAE severity

(A) Schematic representation of AAV-BR1-eGFP construct. (B) Representative immunofluorescence of SC tissue from mice treated with AAV-BR1-eGFP. Tissue was harvested at peak of EAE disease and stained for CD3 (cyan) and laminin (red). Endogenous eGFP is shown in green. Scale bar = 40 μm. (C) Schematic representation of AAV-BR1 constructs. (D) Percentage of ICOSL⁺ ECs and (E) MFI (geometric mean) of ICOSL on brain ECs in wildtype mice treated with AAV-BR1 constructs and two weeks later immunized with MOG/CFA. Analysis was performed at DPI10. Data is pooled from 2 individual experiments with n = 10-15 mice per group. (F-J) A20$^{\Delta CNS-EC}$ or A20$^{fl/fl}$ controls were treated with AAV-BR1-shIcosl or AAV-BR1-con as indicated. One week later, mice were treated with TAM and AT-EAE was induced four weeks later (n = 5-7 mice per group). (F) Clinical signs were monitored daily and are shown as mean clinical scores +/- SEM. (G) AUC, (H) day of onset and (I) score at DPT7 analyses from data shown in (F). (J) Flow cytometric analysis of CD4⁺ CD45.1⁺ transferred T cells in the SC at DPT18. (K-O) Wildtype mice were injected with AAV-BR1 constructs. Two weeks later, mice were immunized with MOG/CFA. (K) Clinical signs were monitored daily and are shown as mean clinical scores +/- SEM. Data is pooled from 2 independent experiments with n=12-15 mice per group. (L) AUC and (M) day of onset and (N) score at day post immunization (DPI) 13 analyses of clinical course shown in (K). (O) Flow cytometric analysis of CD45⁺ in the SC at DPI30. Statistical significance was determined by two-tailed unpaired Student's t-test (L-O) or ordinary one-way ANOVA with Tukey's multiple comparisons test (G-J). ns = not significant, * $p<0.05$, ** $p<0.01$.
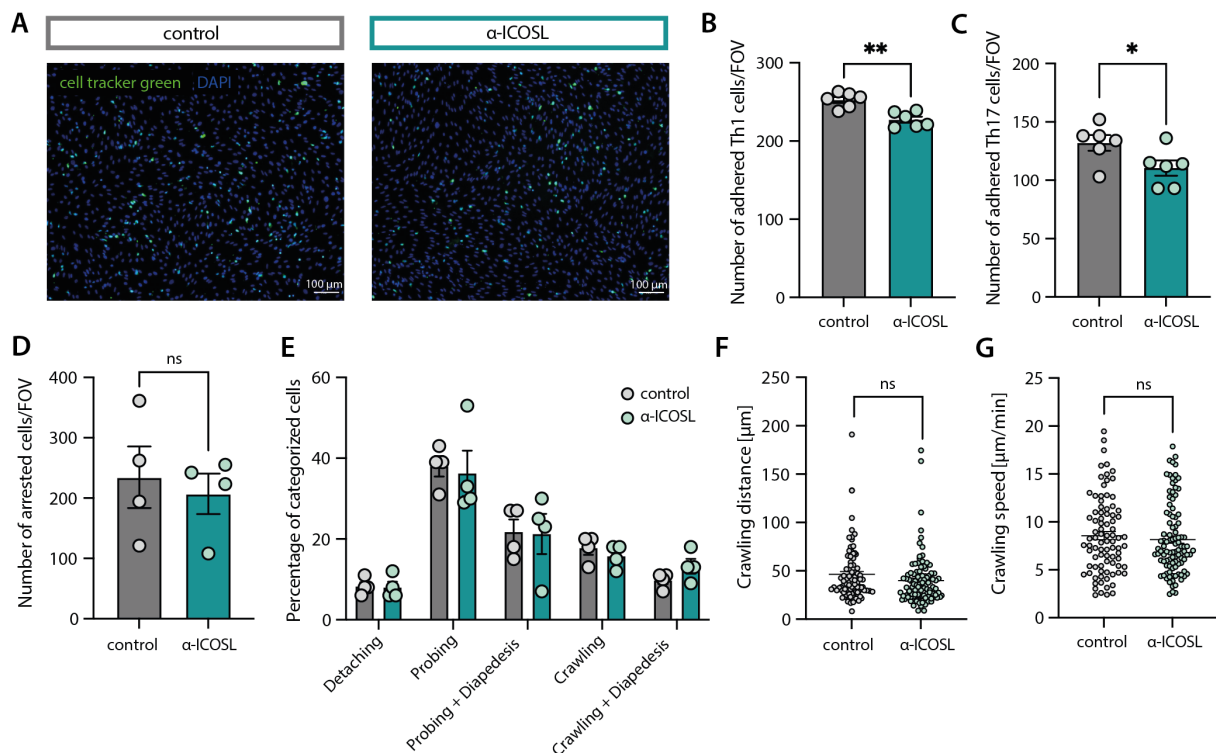
1084

Figure 7: ICOSL regulates T cell adhesion to pMBMECs

(A-C) Static adhesion assay of T cells on pMBMECs. pMBMECs were stimulated with IL-1β for 72 h and incubated for 30 min with α-ICOSL or control antibody. T cells were labelled with CellTracker™ Green CMFDA dye and added for 30 min to the pMBMECs on a shaking platform. After washing, images were taken and adhering cells were counted. Data is representative for 2 individual experiments with n = 6 per group. (A) Representative microscopic images of 2D2 Th1 cells (green) adhering to the pMBMEC monolayer (nuclear stain blue, DAPI). (B) Quantification of number of adhered 2D2 Th1 cells per field of view (FOV). (C) Quantification of number of adhered 2D2 Th17 cells per FOV. (D-G) Analysis of T cell post-arrest behavior on pMBMECs. Data is pooled from 4 individual experiments. pMBMECs were stimulated with IL-1β for 72 h and incubated for 30 min with α-ICOSL or control antibody. 2D2 Th1 T cell post-arrest behavior was assessed by live cell imaging under physiological flow. (D) Number of arrested Th1 cells per FOV. (E) Quantification of T cell post-arrest behavior. Each category is shown as fraction of the sum of the categorized cells. (F) Crawling distance of T cells that successfully completed diapedesis on IL-1β-stimulated isotype or α-ICOSL treated pMBMECs under flow conditions during 20 min observation time shown in μm. (G) Crawling speed of T cells that successfully completed diapedesis on IL-1β-stimulated isotype or α-ICOSL treated pMBMECs under flow conditions shown in μm/min. Data in (F) and (G) is pooled from 4 individual experiments with n = 86-102 tracks analyzed. Data was analyzed using two-tailed unpaired Student's t-test (B-D, F, G) or two-way ANOVA with Šidák's multiple comparison test (E). ns = not significant, * $p < 0.05$, ** $p < 0.01$.